CWP-461
May 2003

Multiple scattering of surface waves

Kasper van Wijk

— Doctoral Thesis —
Geophysics

Defended on May 1, 2003

Committee Chair:	Prof. E. Craig Simmons
Advisor:	Prof. John A. Scales
Committee members:	Prof. Roelof K. Snieder
	Prof. Michael L. Batzle
	Prof. Thomas M. Boyd
	Prof. David M. Wood

Center for Wave Phenomena
Colorado School of Mines
Golden, Colorado 80401
(1) 303 273-3557

Abstract

Multiple scattering of elastic waves in disordered media offers a complexity of the wave field that is challenging to unravel. The subsurface is an example of a medium with disordered inhomogeneity at all scales. However, because waves that bounce around for a long time and/or distance sample the Earth well, they potentially offer great insight into the structure of the subsurface.

A surface wave scattering model is presented to aid the understanding of multiple scattering. Advantages of this model include accessibility of the wave field within the scattering medium, tunable scattering strength, availability of phase and amplitude information, and the relative longevity of surface waves. Accompanied by a state-of-the-art non-contacting data acquisition scheme, this system proved ideal for unveiling the effects of multiple scattering.

When a pulse is launched in a strongly scattering medium, it travels ballistically at first, but turns diffusive as multiply scattered waves interfere with the incident pulse. Radiative transfer has proven to describe both the transmission of the coherent pulse through the scattering media, as well as the diffusive energy that is dominant at later times. Advances in the the understanding of radiative transfer theory both experimentally, as well as theoretically, make it possible to quantify bulk properties of this scattering medium, including independent estimates of scattering attenuation and intrinsic absorption and energy velocity. Preliminary studies in full-waveform sonic logging show potential of such an analysis in terms of radiative transfer.

Small amplitude variations caused by scattering were also observed and confirmed by spectral-element numerical simulations. These included body-wave precursors to the dominant surface waves and flexural resonance of the scatterers.

As an application of this work, a model is presented that proved to be a successful test in applying a wave-equation based method to image, predict and subtract scattered waves, when the interest is in other events than the scattered field.

I'm pickin' up good vibrations
B. Wilson and M. Love
SMiLE, 1966

Table of Contents

Chapter 1

Introduction

In geophysics many studies have been devoted to the topic of scattering from inhomogeneities in the Earth. Of course, we heavily rely on impedance contrasts in the Earth to reflect seismic energy back to the surface, but heterogeneity on a scale smaller than the dominant wavelength is known to influence the characteristics of the seismic signal. For instance, O'Doherty & Anstey (1971) show that reflections within thin layers alter the frequency content of the transmitted pulse, while Backus (1962) found that thin layering, or any preferred orientation of scatterers, makes the seismic velocities angle-dependent (i.e., anisotropic). In Kennett (1984), scattering from heterogeneity in the Earth's crust is shown to transfer energy from the vertical component to the horizontal components. Could this be an early report on a now well-known characteristic of multiple scattering called equipartition (Hennino *et al.*, 2001)? In addition, the scattering of energy due to inhomogeneities in the subsurface is known to attenuate the coherent signal (often referred to as the *first arrival* or *ballistic peak*). This mechanism for attenuation is coupled to intrinsic absorption. Attempts to decouple these for earthquake measurements by Wu (1985), Wu & Aki (1985) and Wu & Aki (1988) were noble and maybe ahead of their time, but hindered by limited data, both in bandwidth, as well as coverage.

This thesis is a study of multiple scattering of surface waves. While multiple scattering of elastic waves in the Earth is a growing topic of research (e.g., Margerin *et al.*, 1999; Hennino *et al.*, 2001; Wegler & Lühr, 2001; Campillo & Paul, 2003), much of its characteristics are still ill defined. The goal is to show that understanding multiply scattered energy can aid our understanding of the disordered systems like the Earth. In practice, however, exploiting multiply scattered waves to make inferences about a medium can be far more complicated than using single-scattering theory such as the Born approximation. In geophysics, nearly all data processing algorithms are based on single scattering theory (Aki & Richards, 1980), but a highly heterogeneous near-surface (Campman *et al.*, 2003), crust (Campillo *et al.*, 1999), and the boundary between core and mantle (Earle & Shearer, 1997; Margerin *et al.*, 1999) provide coherent and diffuse signal. In contrast, human tissue is such a strong scatterer of light that only diffuse (i.e. multiply scattered) light can be measured (Boas *et al.*, 1995).

A solid block of aluminum contains a number of surface wave models. Each face of the block represents a model with a certain level of complexity in surface wave propagation. In a way, this block is a mini-laboratory for the study of surface waves. Overall, each face of the block is large compared to the dominant wavelength, while surface scatterers are smaller than a wavelength. The smooth face of the block is used to determine the material and

the model is on length scales beyond a mean free path, and the microscopic scale is much smaller than that, the mesoscopic regime covers the length scale around one mean free path. Energy propagation in this regime is described by the theory of radiative transfer of energy.

1.1 Wave propagation in (grooved) aluminum

Chapter 2 concerns the theory of Rayleigh waves in a homogeneous elastic half-space and experiments in a (finite) aluminum block with and without a single groove. Both the end of the block and the groove diffract surface waves to body waves, but the finite depth of the groove makes reflection and transmission of the Rayleigh wave frequency dependent. In addition, the non-contacting data acquisition is introduced. Much experimental surface wave research is done in non-destructive testing, where one looks for small cracks in materials (see Hess, 2002, for an overview), but also in geophysics where surface waves are used in tomographic inversion for the structure of the Earth (Dahlen & Tromp, 1998), the influence of topography on seismic waves is tested (e.g., Komatitsch *et al.*, 1999) and dispersion curves of ground-roll are used to invert for layered models in near-surface geophysics (e.g., Xia *et al.*, 1999).

1.2 Multiple scattering at the macroscopic scale

To understand the different regimes of multiple scattering, describing the propagation of energy and their transitions, it is extremely useful to have a medium in which the scattering properties can be easily adjusted. For example, with phonon scattering one can control the mean free path via the temperature (Wolfe, 1998). If the mean free path is greater or equal to the size of the sample, then the phonons propagate ballistically. The more scattering between source and detector, the more diffusive the propagation. Chapter 3, based on Scales & van Wijk (1999, 2001), introduces such a surface model in our mini-laboratory. Here we use a face of the block with many grooves per wavelength. Waves propagating parallel to the grooves propagate nearly attenuation and dispersion free, but waves propagating normal to the grooves are dispersed and exponentially attenuated with distance as waves bounce between the grooves. This means that energy is transferred from the direct pulse to later times. This tail of energy is called the multiple-scattering coda. We measure this attenuation length and show that there is, in addition, a scattering induced anisotropy in the group and phase velocity.

By varying the source-receiver orientation with respect to the grooves and the distance between source and receiver, we are able to map out the transition from ballistic to diffusive energy propagation and measure the angle-dependent macroscopic properties of the medium, such as the group velocity, and the scattering mean free path. Finally, the observations around a mean free path are fit in the macroscopic description of diffusion.

Chapter 2

Surface waves in theory and experiment

2.1 Summary

An aluminum block serves as a mini-laboratory for surface wave studies. It is large compared to the dominant wavelength and the aluminum behaves nominally elastic for our purposes. Grooves, which are small compared to the source wavelength, reflect, transmit and even convert the incoming surface wave energy to body waves. However, before we look at complicated interference of surface waves scattered on the face with a multitude of grooves, let us examine the theory of Rayleigh waves, their characteristics on a smooth face of the aluminum laboratory, and finally, on the face with a single groove.

2.2 Introduction

Quantifying the results of surface-wave scattering from lateral variations is of direct interest in geophysics. Scattering caused by topographic variations introduces dispersion of the early arriving energy, which competes with dispersion related to horizontally layered structures. In addition, in global seismology, surface topography or sedimentary basins can trap seismic energy (e.g., Komatitsch *et al.*, 1999), posing seismic hazard, while in exploration geophysics topography needs to be accounted for in terms of static corrections (e.g., Campman *et al.*, 2003).

The aluminum surface wave laboratory is 28 cm $\times$ 23 cm $\times$ 21.5 cm. A transducer mounted on the surface of an aluminum block excites surface waves. For a detailed analysis of the source characteristics, I refer you to Appendix A. The scattered wave field is recorded with a laser Doppler vibrometer. This entire setup is positioned on a vibration isolation table. This type of non-contacting data acquisition is used on a regular basis in non-destructive testing (see Hess, 2002, for an overview of the literature).

2.3 Rayleigh waves in an elastic and isotropic half-space

Navier's equation, the homogeneous equation of motion in a homogeneous elastic half-space, follows from a balance of forces (e.g., Aki & Richards, 1980):

$$(\lambda + \mu)\,\boldsymbol{\nabla}\,(\nabla \cdot \mathbf{u}) + \mu \nabla^2 \mathbf{u} = \rho \ddot{\mathbf{u}}, \tag{2.1}$$

where $q^2 = k^2 - k_p^2$, $s^2 = k^2 - k_s^2$ and (A, B) are arbitrary constants. With the conditions that at the boundary of the elastic half-space the stresses are zero: σ_{zz} and $\sigma_{xz} = 0$, we can write B in terms of A, and find the characteristic relation between the k, s and q to be

$$4k^2qs - \left(k^2 + s^2\right)^2 = 0. \tag{2.10}$$

In terms of velocities, this is

$$\left(2 - \frac{c^2}{v_s^2}\right)^2 = 4\sqrt{1 - \frac{c^2}{v_p^2}}\sqrt{1 - \frac{c^2}{v_s^2}}, \tag{2.11}$$

where $c = \omega/k$. This equation is known as the Rayleigh equation, named after J. W. Strutt, Lord Rayleigh, who first published this in 1885 (Strutt, 1885). Mathematically, this equation has six roots for c, but as the Poisson's ratio lies between 0 and 0.5, and we know that the surface wave has to decay with depth, each elastic isotropic medium has one Rayleigh wave with a velocity c_R that ranges between 0.87 to 0.96 times the shear wave velocity, depending on the Poisson's ratio of the medium. Once c_R is known, we can determine individually the inhomogeneous longitudinal and shear wave components from equation (2.9) that are in a Rayleigh wave:

$$\phi = -A\exp(i(kx - \omega t) - qz) \quad \text{and} \quad \psi = iA\frac{2kq}{k^2 + s^2}\exp(i(kx - \omega t) - sz). \tag{2.12}$$

If we know v_p and v_s, the variables s, q are now known and A is a scaling term. From these equations one can see that the shear component is 90 degrees out of phase with the compressional component, due to the factor i. This causes the famous elliptical polarization of the Rayleigh wave. Worth pointing out is that even though the assumed model here is 2D, the out-of-plane shear-component of the vector potential turns out to be zero in a 3D analysis. Finally, equation (2.12) shows that the polarizations decay exponentially with depth, governed by q and s, respectively. Because s and q are proportional to frequency, low frequency Rayleigh-wave components sample the medium to a greater depth than high frequency components.

2.4 Source and receiver in the laboratory

This Section discusses in general terms the excitation and detection of Rayleigh waves in aluminum in the laboratory, but a much more detailed analysis of the source properties is laid out in Appendix A.

2.4.1 The Rayleigh wave source

In the laboratory, waves are exited with a piezo-electric crystal that has the ability to convert a voltage to a mechanical force. This crystal is mounted on a Lucite wedge and this wedge is mounted on the aluminum model. The angle of the wedge is such, that the horizontal component of the P-wave speed in Lucite matches the Rayleigh wave

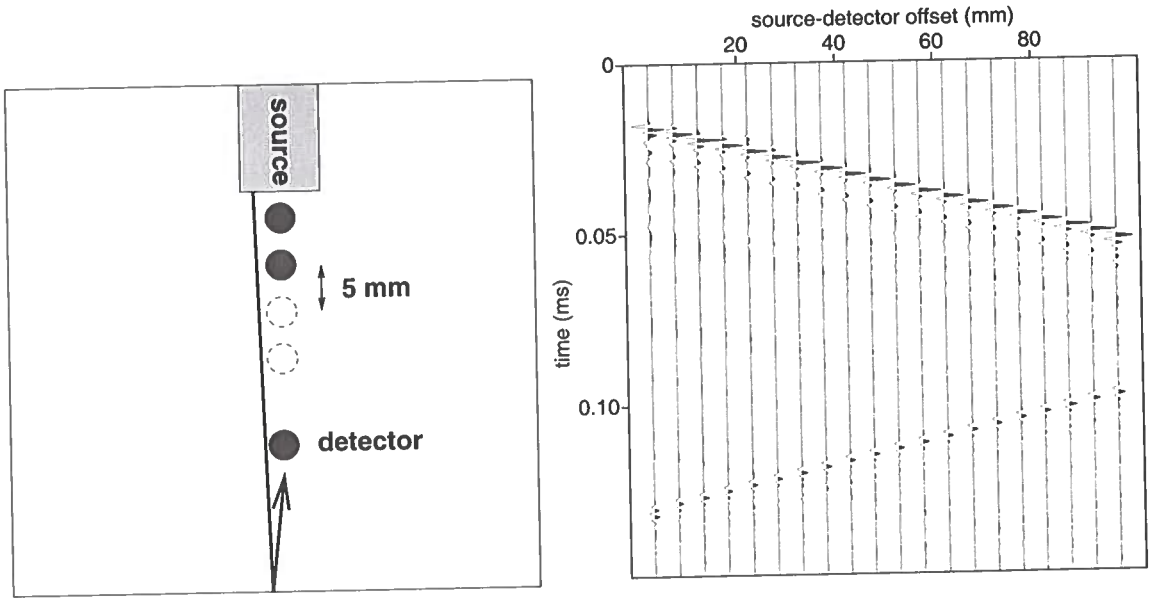

Figure 2.1. Top-view of the experimental configuration (left) on the smooth face of aluminum. The shaded box represents the source and the circles represent 20 equi-spaced detector locations. The wave field for each detector is shown on the right. The spot-size of the interferometer beam has a diameter of 1 mm, the source is 42 mm wide, and the dominant wave-length is on the order of 1 cm.

the direct wave, because energy is diffracted to body waves at the edge of the block. Since the amplitudes of the direct arrival (or of the reflection) vary insignificantly with source-detector distance, we consider the aluminum block to behave elastically and thus neglect intrinsic absorption.

The phase velocity of the Rayleigh wave on the smooth face of aluminum is experimentally determined from the move-out of a particular phase of the wave field, as a function of distance. Figure 2.2 shows the picks of the maximum energy in each trace and the regression through the picks. This measured phase velocity of the Rayleigh wave is $v_R \approx 2870 \pm 5$ m/s. Even though the documented material properties vary from one aluminum to the next (Anderson, 1989), with the knowledge of v_p and v_s from transmission measurements, equation (2.11) predicts the Rayleigh wave speed to be $v_R \approx 2864$ m/s.

2.6 When a surface wave meets a groove

A computer controlled milling machine etched a single 1-mm wide and 2.75-mm deep groove on one face of the aluminum block. When a Rayleigh wave encounters this groove, part of its energy is reflected and part is transmitted. However, just like the edge of the block, the groove diffracts energy to body waves as well. The magnitude of these parts is

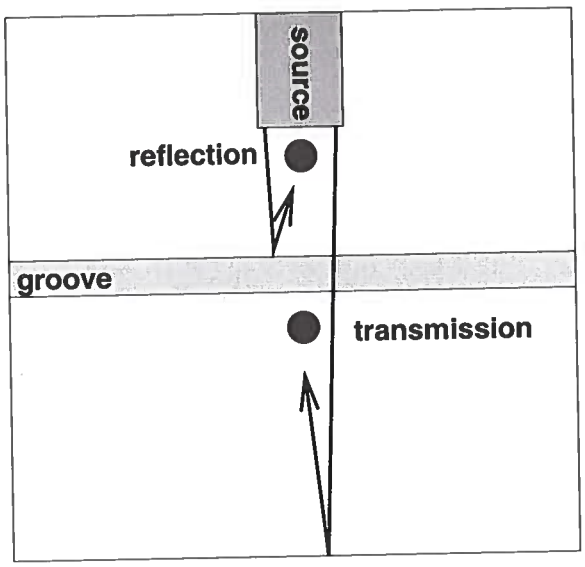

Figure 2.3. Top-view of the experimental configuration. The circles represent detector locations. The spot-size of the interferometer beam has a diameter of 1 mm, the source is 42 mm wide, and the dominant wave-length is on the order of 1 cm. The recorded wave field at these detectors is depicted in Figure 2.4.

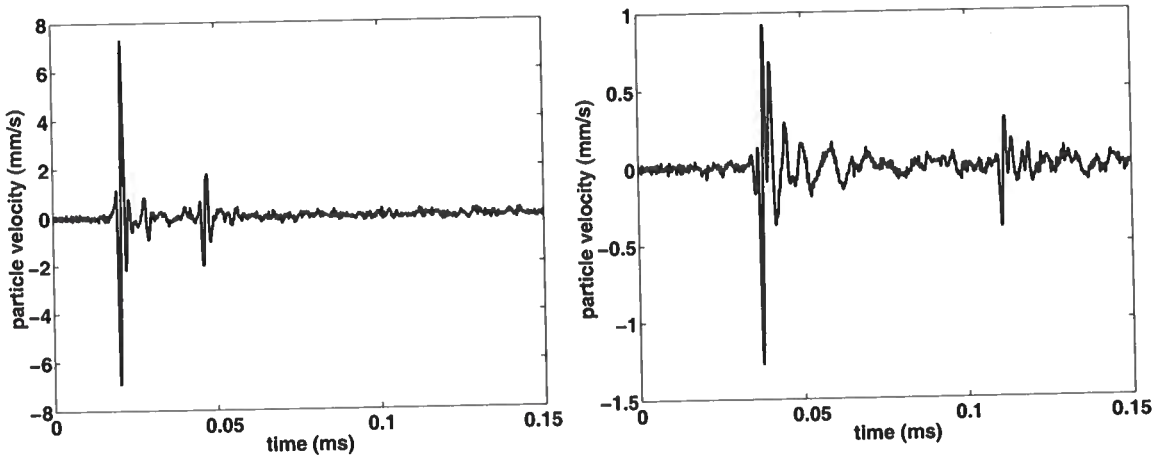

Figure 2.4. Reflection (left) and transmission (right) for a single groove. The primary peaks are the direct arrival. In the left panel, the secondary peak is a reflection from the groove, while in the right panel this secondary peak is the reflection from the end of the block.

Chapter 3

Multiple scattering at the macroscopic scale

3.1 Summary

This Chapter describes wave propagation on a face of our aluminum laboratory with many grooves. Waves traveling parallel to the grooves do not encounter the scatterers, but as I rotate the angle between the direction of propagation and the groove orientation, scattering gets stronger, causing attenuation, dispersion and a decrease in seismic velocities. Ensemble measurements of wave propagation perpendicular to the grooves are used to determine the scattering mean free path. Energy propagation at source-detector distances of a mean free path or beyond should – by definition – start to show diffusive behavior. The macroscopic description of diffusion of energy is confirmed by fitting the data to the Green's function for the 1D diffusion equation.

3.2 Introduction

The influence of multiple scattering in wave propagation measurements can be seen in many ways. There are subtle, long-wavelength effects such as anisotropy (if the scatterers are aligned) and attenuation (as energy is shifted from the ballistic pulse into the multiple-scattering coda) (Groenenboom & Snieder, 1995). These effects are well known in seismology (e.g., Backus, 1962; Aki & Chouet, 1975; O'Doherty & Anstey, 1971) and have been used to interpret effective material properties from macroscopic measurements. However, in most cases the same phenomenon can be looked at from different points of view (such as ballistic propagation, diffusion or radiative transfer) depending, for example, on the wavelength of the probing beam relative to the size of the disorder and on the distance propagated. To understand these different regimes, a surface wave model is presented in which the scattering properties are easily adjusted.

3.3 The grooved aluminum model

On one face of the aluminum block, a computer-controlled milling machine etched a Fibonacci sequence[1] of aligned linear grooves (Figure 3.1). These sequences are frequently

[1]From *Liber Abbaci*, 1202 but revised in 1228. meaning The Book of the Abacus (or The Book of Calculating). One of the problems in this book was about reproducing rabbits, which introduced the series 1,1, 2, 3, 5, 8, ... It was much later (around 1870) that Lucas named this series of numbers after Fibonacci.

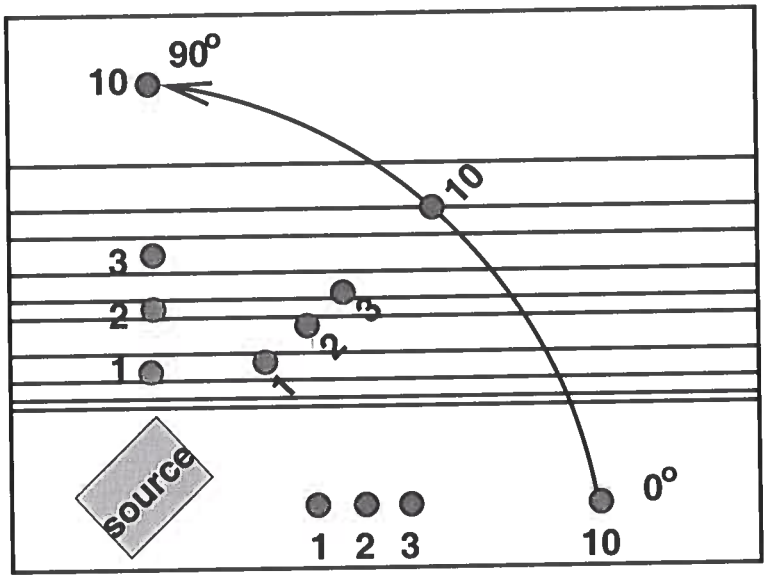

Figure 3.2. Top-view of the experimental configuration that measures the wave field at 10 source-detector offsets for 10 angles between the source-detector line and the grooves, ranging from 0 to 90 degrees.

3.4 A tunable multiple-scattering system

The basic measurement consists of the vertical component of particle velocity measured at 1-cm increments or *offsets*, along a line extending perpendicularly from the transducer front to a maximum offset of 10 cm. Such a measurement is called a *constant-angle section.* The line along which the measurements are made defines an angle relative to the orientation of the grooves. Constant-angle sections range from 0 to 90 degrees, with 10-degree spacing; 0 degrees being parallel to the grooves. Thus there are a total of 100 traces (10 angles and 10 offsets). The experimental configuration is sketched in Figure 3.2.

Figure 3.3 contains the wave fields for propagation parallel to the grooves. It shows that propagation at zero degrees with the grooves is essentially identical to propagation on the smooth surface of aluminum in Figure 2.1; both are nominally attenuation- and dispersion-free. An exception is the last trace, where the detector was positioned on the edge of the surface. There, a complicated super-position of the surface wave and the diffraction at the corner alter the measured wave field. However, as the angle of the propagation increases, scattering becomes significant. Figure 3.4 the source-detector line at 50 degrees with the grooves: an intermediate scattering strength. In this constant-angle section one can see dispersion and attenuation of the early arrivals, and multiple-scattered energy arriving at later times. Figure 3.5 shows the transition from ballistic propagation to strong multiple-scattering as the angle between surface wave propagation and the grooves is increased.

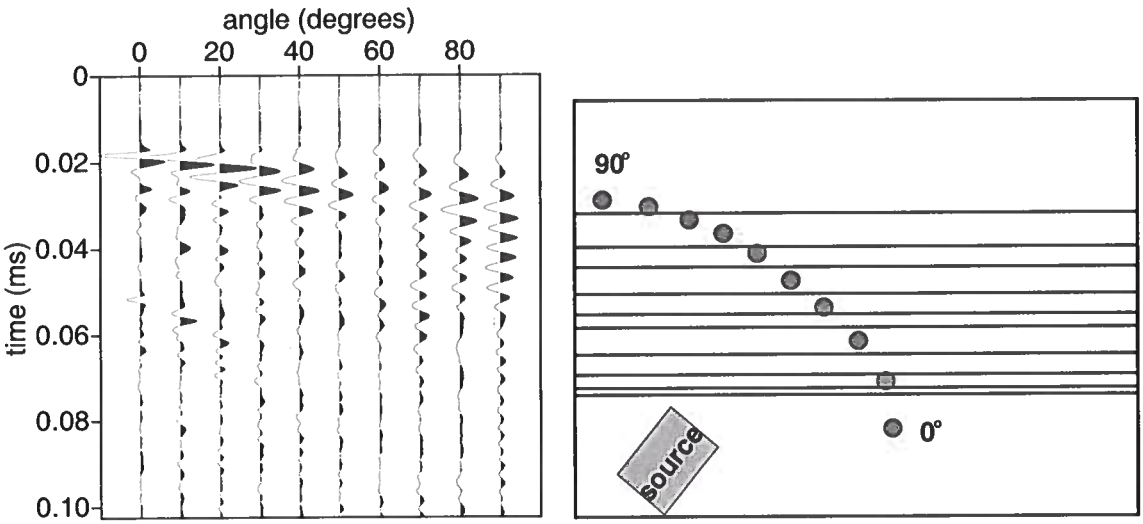

Figure 3.5. A constant-offset section (5 cm); that is, variable angles for a fixed source-receiver distance.

In the absence of scattering, the dominant frequency is that of the source wavelet; around 400 kHz. However, scattering reduces the high frequency power in the data in two ways. First, because the 2.75 mm-deep grooves scatter the shallower traveling high frequencies more effectively, they are poorly transmitted. Second, the interference of multiples in a cyclic system (aluminum/air) is known to reduce the frequency of the transmitted pulse. Basically, the multiples trailing in the forward direction have the same polarity, because they have changed sign twice at a boundary between aluminum and air (e.g., O'Doherty & Anstey, 1971; Mateeva, 2001). This means pulses of the same polarity arrive within a dominant wavelength, broadening the cumulative wavelet.

3.4.1 Group velocity vs. scattering strength

The longer effective path lengths of the multiply-scattered waves result in a significant slowing of the energy propagation. To estimate this group velocity as a function of angle, the data is sorted into constant-angle sections and the energy envelopes of each trace are computed. The peaks of these envelopes were picked automatically and the times taken to be the arrival times of the pulse. This gives an arrival time for each offset, the set of which were fit with a straight line to arrive at the group velocity (Figure 3.6). The error bars are 98% coverage intervals from the regression. Destructive interference or mode-conversion causes intensities from 60-80 degrees to be weaker, making the error bars in the group velocity estimate larger. The group velocity in the strongest scattering case (90 degrees) is discussed in Appendix C.

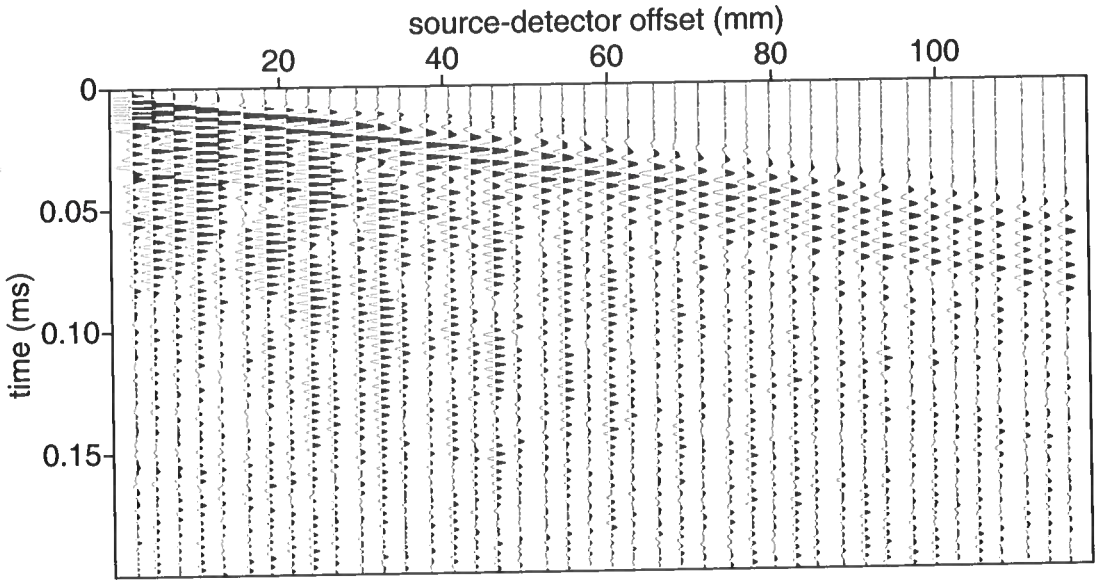

Figure 3.7. The wave field recorded on the grooved aluminum surface on each of the first 42 non-grooves.

3.5 Strongest scattering

Figure 3.7 contains the records of wave propagation normal to the grooves. The source is located before the groove sequence and the detectors are between the first 42 grooves. This area of aluminum is called a non-groove. Signal for the first traces in Figure 3.7 are clipped in amplitude, so that the traces with a larger source-detector separation show ample signal. This illustrates the strong attenuation of the first arrival, caused by scattering from the grooves; not only is energy diffracted to body waves, it is also delayed by bouncing around between grooves. This energy at late times is often called the coda.

The left panel of Figure 3.8 shows the peak amplitude of the first pulse as a function of distance from the source. The decay is well fit by an exponential. The decay length will vary according to the properties and distribution of the scatterers; in this particular case the $1/e$ decay length is about 25 mm. For a quasi-1D system such as this, this decay length can be taken to be the localization length (Scales & van Vleck, 1997). The right panel of Figure 3.8 shows the arrival time of a particular surface wave phase as a function of the source-receiver offset. The slope of the best fitting straight line gives an estimate of the phase velocity. For propagation on the smooth face, or for propagation parallel to the grooves, regression yields a phase velocity of 2870 ± 5 m/s, whereas for propagation normal to the grooves the phase velocity is 2801 ± 14 m/s. Since the depth of the medium is many wavelengths and the medium itself is homogeneous, except for the grooves (which

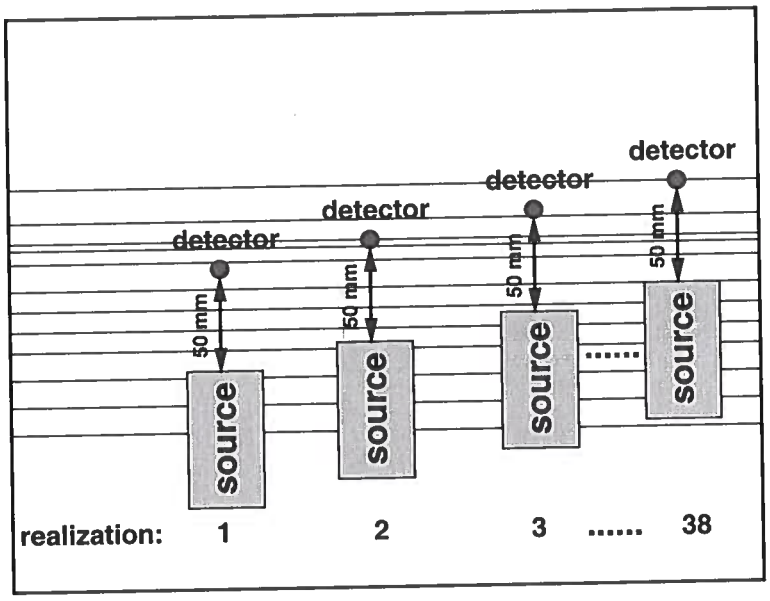

Figure 3.9. Top-view of the experimental configuration to measure the wave field at 38 locations at a fixed source-detector offset of 5 cm on the block.

medium filled with random scatterers, the total and coherent intensities are expected to decay exponentially as (see Ishimaru, 1997), section 14-3): $I_t(x) = I_0 \exp(-x/\ell_a)$ and $I_c(x) = I_0 \exp(-x/\ell_a) \exp(-x/\ell_s)$, where ℓ_a and ℓ_s are the absorption and scattering mean free paths, respectively. Therefore, the ratio of these two intensities decays exponentially, depending only on the scattering mean free path (De Rosny & Roux, 2001):

$$\frac{I_c(x)}{I_t(x)} = \exp(-x/\ell_s) = \exp(-vt/\ell_s) = \exp(-t/\tau_s), \tag{3.2}$$

where v is the group velocity and τ_s is the scattering mean free time.

Numerically, the coherent intensity I_c is the intensity of the average trace, while the total intensity I_t is the average of the intensities of the individual traces. The ratio of I_c to I_t is shown in Figure 3.11. Fitting an exponential to the portion of the curve after the coherent arrival (about 30 μs), the mean free time $\tau_s = 24$ μs. Since this measurement is for propagation at 90 degrees with respect to the grooves, the group velocity is around 2 mm/μs, which gives a mean free path of just under 5 cm. Thus we are in a regime in which the wavelength is large compared to the size of an individual scatterer, but small compared to the mean free path; while we have measurements with source-detector offsets as large as 2 mean free paths. In this sense one observes here the transition from ballistic to diffusive propagation. With this estimate of the scattering mean free path, the coherent intensity decays exponentially with an absorption length $\ell_a \approx 50$ mm. This absorption describes the loss of energy from diffractions off the bottom of the grooves.

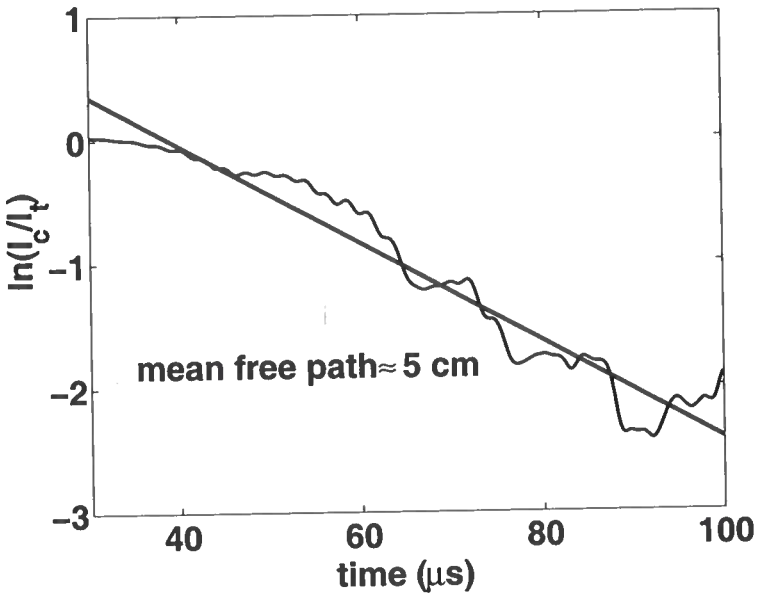

Figure 3.11. Ratio of coherent to total intensities averaged over the ensemble of realizations. The curve decays after the coherent arrival. This decay is fit with an exponential the decay constant of which is the mean free time; in this case, 24 μs.

To get some idea of whether the total intensity behaves diffusively at 5 cm offset, as is suggested by our estimate of the mean free path, we fit the ensemble-averaged total intensities with an analytic model associated with propagation in a homogeneous diffusive, absorbing medium. We included absorption to account for diffraction losses off the grooves. The Green's function for this model is given by

$$I_t(x,t) = (4\pi Dt)^{-1/2} \exp\left(-\frac{x^2}{4Dt} - D\kappa^2 t\right), \tag{3.3}$$

where $\kappa = 1/\ell_a$ is the absorption coefficient, D is the diffusion constant and x is the propagation distance. This solution is derived in Appendix B.6. A fit to the data is shown in Figure 3.12.

3.6.1 Discussion

This fitting to the diffusion equation alone, cannot determine D, explicitly; the propagation distance is not well-defined since in the real experiment the waves propagate ballistically for some distance, whereas the model is for a homogeneous diffusive medium. However, we can get a rough estimate of the diffusion constant as follows. First $D = v\ell_{tr}/d$ where v is the transport velocity, ℓ_{tr} is the transport mean free path and d the dimension of the

Chapter 4

Multiple scattering at the mesoscopic scale

4.1 Summary

Here we show detailed measurements of wave propagation in a 1D strongly scattering medium that fit the theory of radiative transfer for both early times (ballistic propagation) and late times (diffusive propagation). Using the radiative transfer model we are able to estimate the energy velocity and both the scattering and absorption mean free paths.

4.2 Introduction

When waves propagate through a medium they encode information about the properties of that medium. The information from multiply scattered waves has a very different character than that associated with directly propagating or singly-scattering waves. Consider two examples. A normal mode or standing wave can be thought of as the superposition of traveling waves that repeatedly sample a finite medium (by reflection from or propagation around boundaries). Thus small changes in the size or properties of the medium are amplified by each pass of the traveling waves; this amplification leads to the exquisite precision of spectroscopy, allowing one to infer properties that would be completely undetectable with directly propagating waves (Zadler *et al.*, 2003). On the other hand, suppose a wave passes through a cloud of similar scatterers; if some property of the scatterers changes, then this effect is repeatedly imparted on the multiply-scattered wave, making it potentially observable even when the perturbation of a single scatterer is unresolvable (Snieder *et al.*, 2002; Lemieux *et al.*, 1998; Cowan *et al.*, 2002).

Propagation of strongly scattering surface waves is analyzed in this Chapter using model of radiative transfer. Radiative transfer has its origins in the kinetic theory of gases and is sometimes referred to as the Boltzmann transport equation in honor of its earliest proponent. In the earth sciences, it first appeared within the context of light propagation through the atmosphere (Schuster, 1905). Recently, geophysicists have begun to address the applicability of radiative transfer to multiply-scattered seismic waves (e.g., Hennino *et al.*, 2001; Campillo & Paul, 2003; van Wijk *et al.*, 2003b; Wegler & Lühr, 2001; Wu & Aki, 1988).

By squaring a wave field and averaging over many realizations of random disorder, the phase information of the underlying wave field is lost. What remains is the average intensity. Radiative transfer is a phenomenological theory for the spatial and temporal evolution of a wave field's average intensity. The theory's strengths lie in the ability to provide statistical

Figure 4.2. Side-view of paths for energy in grooved aluminum. Scattering of the incident surface wave causes loss of the transmitted field (left), but energy can be gained by being re-reflected in the direction of propagation (right).

the characteristic 1/e decay distance, called the extinction mean free path ℓ^*. The difference from the loss to body wave diffraction is that the scattered energy stays in our 1D surface model. In fact, when the reflected surface wave encounters another groove, it can reflect once more, and travel – delayed and weakened by two reflection events, but still – in the original direction of the incident field (Figure 4.2. This means that scattering is both a loss and a gain term when we make up the energy balance. Note the analogy to body wave propagation in thin layers, where O'Doherty & Anstey (1971) show that the transmitted wave is shaped by *peg-leg* multiples; waves that scattered an even number of times in layers thinner than the dominant wavelength (Banik *et al.*, 1985; Shapiro & Zien, 1993). Finally, note that scattering and absorption enter the energy balance in fundamentally different ways. This leads to the ability to separate these effects in the laboratory, later in the Chapter.

Radiative transfer takes the energy balance described above for a medium with a random distribution of scatterers, and states that the average intensity as a function of time and place, takes the following form:

$$(\partial_t + v \cdot \nabla)\,\text{intensity} = \text{source} - \text{loss} + \text{gain}. \tag{4.1}$$

The left-hand side of equation (4.1) is the total time derivative of the intensity. On the right-hand side, loss and gain mechanisms in addition to sources determine the dynamic behavior. In the absence of loss or gain, this equation becomes the advection, or one-way wave, equation.. Using the same form as equation (4.1), the scalar (no mode conversions at the scatterers) radiative transfer equation valid for any dimension is

$$\frac{\partial I(\mathbf{r},\Omega,t)}{\partial t} + v\hat{n}(\Omega)\cdot\nabla I(\mathbf{r},\Omega,t) = S(\mathbf{r},\Omega,t) - \frac{1}{\tau_s}I(\mathbf{r},\Omega,t) - \frac{1}{\tau_a}I(\mathbf{r},\Omega,t) + \frac{1}{\tau_s}\int \frac{1}{\sigma_s}\frac{\partial\sigma_s}{\partial\Omega'}I(\mathbf{r},\Omega',t)\,d\Omega', \tag{4.2}$$

where $I(\mathbf{r},\Omega,t)$ is the intensity, or average squared wave field, at position $\mathbf{r}$ propagating in direction Ω, v is the group velocity of the average (coherent) wave field, $\hat{n}$ is the unit vector in the direction of propagation, and $S(\mathbf{r},\Omega,t)$ is the angle-resolved source function. The differential scattering cross section, $\partial\sigma_s/\partial\Omega'$, describes the exchange of energy traveling from direction Ω into direction Ω'. The characteristic time between these exchanges is τ_s,

Note that a thin bed consists of two interfaces, and hence R_t and T_t are not simple reflection and transmission coefficients. The quantities R_t and T_t can be related to a geometric summation of the interface reflection and transmission coefficients via generalized rays (Aki & Richards, 1980).

Inserting equation (4.7) into equation (4.2), we obtain that

$$\frac{\partial I(x,\Omega,t)}{\partial t} + v\hat{n}(\Omega)\frac{\partial I(x,\Omega,t)}{\partial x} = S(x,\Omega,t) - \frac{1}{\tau_s}I(x,\Omega,t) - \frac{1}{\tau_a}I(x,\Omega,t) + \frac{1}{\tau_s}\int \left[F\delta(\Omega'-\Omega) + B\delta(\Omega'-\Omega-180°)\right] I(\mathbf{r},\Omega',t)\,d\Omega' = \frac{B}{\tau_s}I(x,\Omega+180°,t) - \frac{B}{\tau_s}I(x,\Omega,t) - \frac{1}{\tau_a}I(x,\Omega,t) + S(x,\Omega,t), \tag{4.9}$$

where we have used the fact that $B + F = 1$. Equation (4.9) can be evaluated for the two possible directions in 1D, $\Omega = 0°$ or $180°$. Here, these directions are referred to as right and left, respectively. For simplicity, the total intensity propagating in direction $\Omega = 0°$, $I(\mathbf{r}, 0°, t)$, is represented by I_r, $I(\mathbf{r}, 180°, t)$ is I_l, and the source function is split into S_r and S_l. The coordinate system is defined such that $\hat{n}(0°) = 1$ and $\hat{n}(180°) = -1$. The two equations that describe the propagation of right-going and left-going intensities are

$$\frac{\partial I_r}{\partial t} + v\frac{\partial I_r}{\partial x} = \frac{B}{\tau_s}(I_l - I_r) - \frac{I_r}{\tau_a} + S_r, \tag{4.10}$$

$$\frac{\partial I_l}{\partial t} - v\frac{\partial I_l}{\partial x} = \frac{B}{\tau_s}(I_r - I_l) - \frac{I_l}{\tau_a} + S_l. \tag{4.11}$$

This system of partial differential equations comprises radiative transfer in 1D and has been derived by other methods (Goedecke, 1977). In Appendix B.3, the system of partial differential equations is solved for both I_r and I_l. For now, we solve for the total intensity, $I_t = I_r + I_l$, since this is commonly measured in practice.

Two new quantities emerge from adding and subtracting equations (4.10) and (4.11). In addition to the total intensity, I_t, the net right-going intensity, $I_n = I_r - I_l$, appears. Similarly, the source function can be expressed as its total and net right-going components: $S_t = S_r + S_l$ and $S_n = S_r - S_l$. The result of adding equations (4.10) and (4.11) is

$$\frac{\partial I_t}{\partial t} + v\frac{\partial I_n}{\partial x} = -\frac{I_t}{\tau_a} + S_t, \tag{4.12}$$

Subtracting equations (4.10) and (4.11) yields:

$$\frac{\partial I_n}{\partial t} + v\frac{\partial I_t}{\partial x} = -\frac{2B}{\tau_s}I_n - \frac{I_n}{\tau_a} + S_n. \tag{4.13}$$

From these two equations, we derive a single partial differential equation in terms of what

This effective source can be constructed from the knowledge of the Green's function, P of the homogeneous form of equation (4.16):

$$\frac{\partial^2 P}{\partial x^2} = \frac{1}{v^2}\frac{\partial^2 P}{\partial t^2} + \left[\frac{2B}{v\ell_s} + \frac{2}{v\ell_a}\right]\frac{\partial P}{\partial t} + \frac{1}{\ell_a}\left[\frac{2B}{\ell_s} + \frac{1}{\ell_a}\right]P - \delta(x)\delta(t). \tag{4.20}$$

Note that P is not the Green's function for the total intensity. This equation is a variation of the telegraph equation, there being a zeroth order derivative appearing due to the presence of attenuation. Morse & Feshbach (1953) solve the Green's function of the telegraph equation via a spatial Fourier transform and a Laplace transform over time. Applying the same technique, the Green's function of equation (4.20) can be readily obtained by generalizing their solution:

$$P(x,t) = \frac{v}{2}\exp\left(-Bvt/\ell_s - vt/\ell_a\right) J_0\left(\frac{B}{\ell_s}\sqrt{x^2 - v^2t^2}\right) u(vt - |x|), \tag{4.21}$$

where $u(vt - |x|)$ is the unit step-function, guaranteeing causality. This Green's function only differs from the one for the telegraph equation by the exponential damping factor due to attenuation. The Green's function for the total intensity, denoted I_t, can be expressed in terms of the above Green's function through equation (4.19):

$$I_t = \left[\frac{2B}{v\ell_s} + \frac{1}{v\ell_a}\right]P + \frac{1}{v^2}\frac{\partial P}{\partial t} - \frac{c}{v}\frac{\partial P}{\partial x}. \tag{4.22}$$

Taking the necessary derivatives of P, we obtain for $B \in [0,1]$ and $c \in [-1,1]$:

$$\begin{aligned} I_t(x,t) = \frac{1}{2}\exp(-Bvt/\ell_s - vt/\ell_a)\left[(1-c)\delta(vt+x) + (1+c)\delta(vt-x) + \right. \\ \left. \frac{B}{\ell_s}u(vt-|x|)\left[I_0\left(\frac{B}{\ell_s}\sqrt{v^2t^2-x^2}\right) + \frac{vt+cx}{\sqrt{v^2t^2-x^2}}I_1\left(\frac{B}{\ell_s}\sqrt{v^2t^2-x^2}\right)\right]\right], \end{aligned} \tag{4.23}$$

where I_0 and I_1 are the modified Bessel functions of the zeroth and first orders. These should not be confused with the symbols used for the various intensities (I_t, I_r, I_l, and I_n). A previous result by Hemmer (1961) is obtained from equation (4.23) for the case of an isotropic source ($c = 0$) and isotropic scattering, $B = 0.5$.

The Green's function for the total intensity can be broken up into two parts. The term with the δ-function propagates like a wave and is called the coherent intensity. The rest of the total intensity is referred to as the incoherent intensity. It does not propagate ballistically, and Appendix B.4 shows that at late times it propagates diffusively. Also, Appendix B.3 shows that each Bessel function represents a different direction of propagation for the incoherent energy. The decay of coherent intensity due to scattering, described by the first exponential term in equation (4.23), goes with distance by the factor ℓ_s/B and not ℓ_s. This new length scale, determining the decay of the coherent energy, is called the *extinction* mean free path, ℓ^*. The fact that $\ell^* \neq \ell_s$ is unique to 1D (Paasschens, 1997).

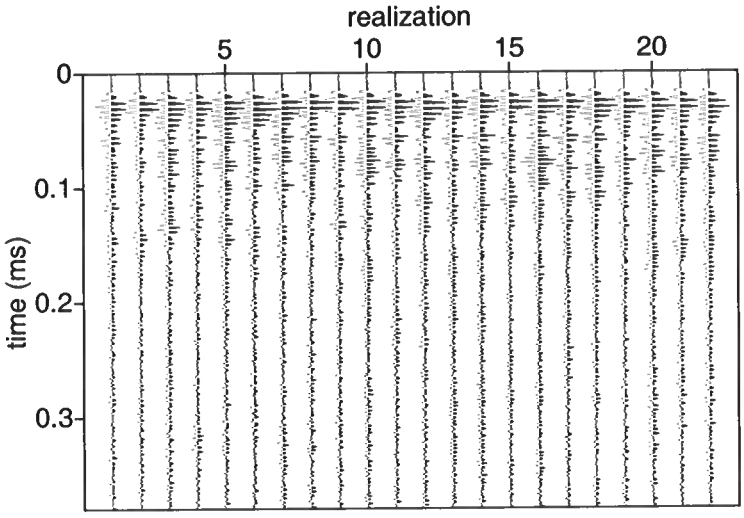

Figure 4.4. Particle velocity at 50 mm source-detector offset for 22 locations of the source-detector pair within the groove sequence.

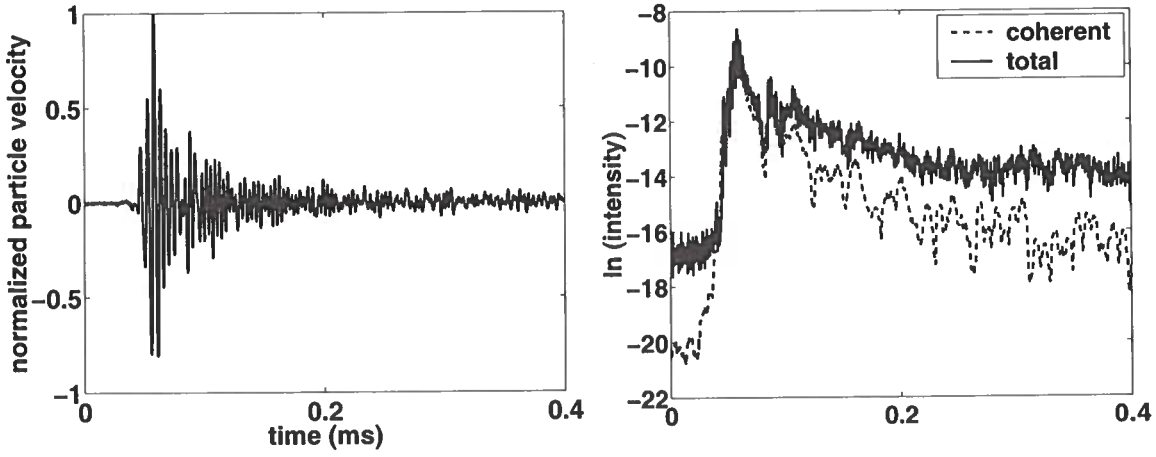

Figure 4.5. Data at 50 mm source-detector offset. The left panel is the average particle velocity for the 22 realizations, and the right panel the natural logarithm of the total and coherent intensity.

The solid lines in Figure 4.6 are the modeled envelopes of the coherent intensity for $\alpha = R/\ell_s + 1/\ell_a = 17.8$ m^{-1} and velocity $v = 1818 \pm 123$ m/s. In our case the coherent velocity equals the transport velocity, even though especially for resonant scattering the velocity of the coherent signal can be significantly higher than the group (transport) velocity (e.g., Page *et al.*, 1996; Kuga *et al.*, 1993; van Albada *et al.*, 1991). The energy of the coherent signal travels dispersively. We therefore model the energy velocity to be a function of frequency: as lower frequency surface waves penetrate the model deeper, they travel for a larger part undisturbed by the scatterers, while higher frequencies are slowed by stronger scattering due to the grooves (Appendix C). The smaller, secondary peak in the coherent intensity is not modeled. This peak is most likely a part of the source wavelet, not accounted for in the model.

Incoherent intensity The incoherent intensity is the coherent intensity subtracted from the total intensity. The data are the solid lines in Figure 4.7. The dashed lines are the result of modeling the incoherent part $I(x,t)$ of equation (4.24):

$$I(x,t) \propto \exp(-\alpha v t) \left(I_0(\eta) + \sqrt{\frac{vt+x}{vt-x}} I_1(\eta) \right). \tag{4.26}$$

Using the energy velocity of 1818 m/s and $\alpha = 17.8$ m^{-1}, the resulting fits in Figure 4.7 are for $R/\ell_s = 11.1$ m^{-1}. We only fit the incoherent signal at intermediate times. At short times the incoherent data are incomplete, and at late times energy comes back into the system from reflections off the back of the model, but in the intermediate time window, the fit describes the average measured incoherent intensity. Note that the incoherent intensity for all three offsets is of equal amplitude in this intermediate window.

Fitting parameters With $R/\ell_s + 1/\ell_a = 17.8$ m^{-1} and $R/\ell_s = 11.1$ m^{-1}, the absorption length is $\ell_a = 0.15$ m. If $R = 0.5$, the mean of the range of possible values, the scattering mean free path is $\ell_s = 0.05$ m. Data at source-detector offsets around ℓ_s, put us in the transitional regime from ballistic to diffusive energy propagation.

Formally, these parameters in the radiative transfer are functions of frequency, since our scatterers have a finite depth, while surface wave frequencies sample different depths of the model. However, the data fit is obtained with an average value of the scattering and absorption parameters. To account for dispersion in the coherent signal, only the energy velocity was treated as a function of frequency.

A direct application in geophysics of radiative transfer modeling is presented in Appendix D: independent estimates of scattering and intrinsic attenuation (Q), are known to double as direct indicators of fluid content in the rock. Partial saturation of the rock has little effect on the scattering properties, but the bulk motion of the fluid attenuates the seismic energy.

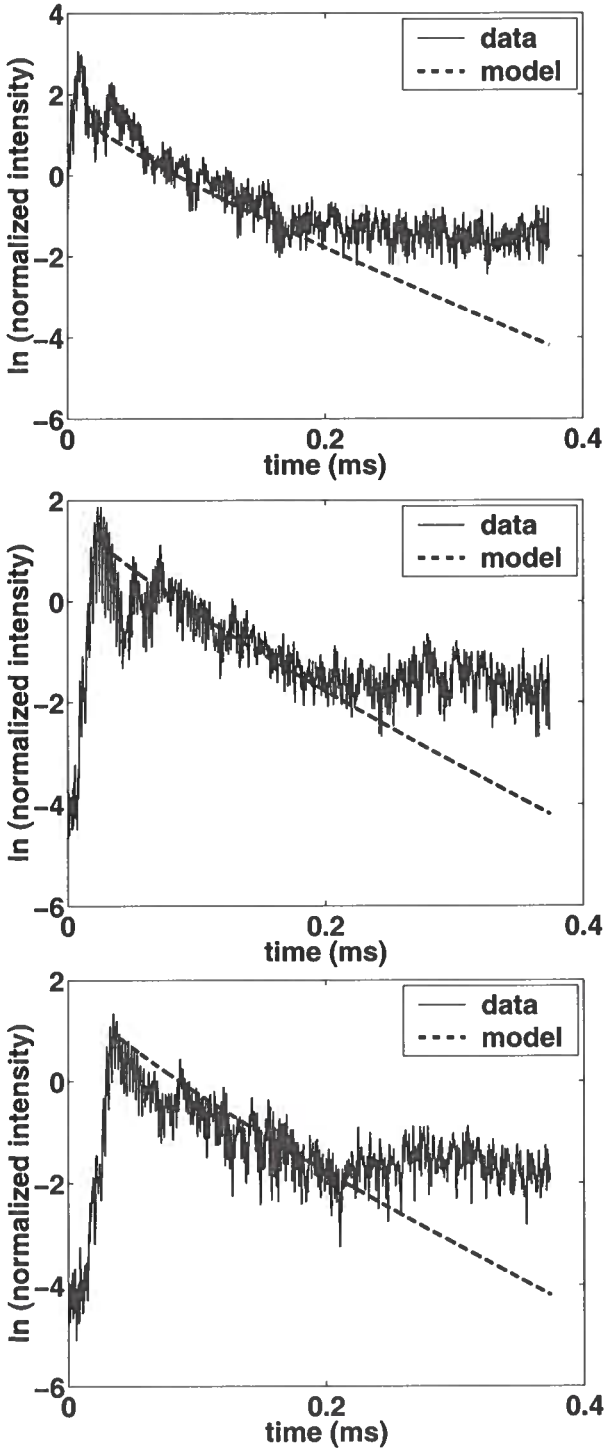

Figure 4.7. Comparison between the measured and modeled incoherent intensities for source-detector offsets of 25 (top), 50 (middle) and 75 mm (bottom).

Chapter 5

Multiple scattering at the microscopic scale

5.1 Summary

Spectral-element simulations of surface wave propagation in our surface wave laboratory provide us with a powerful tool for understanding the complex dynamics of diffraction and scattering. For example, we see in both the experiment and simulation diffracted body waves which are weak precursors to the dominant surface waves; these events may be analogous to diffractions from the Earth's core-mantle boundary. In addition, the numerical code confirms flexural modes of the thin areas of aluminum between grooves and the influence of the source wedge itself on the wave field.

5.2 Introduction

Bulk properties of the propagation, including attenuation and dispersion, were studied to describe the scattering model on the macroscopic scale in Chapter 3, while Chapter 4 shows results of modeling multiple scattered data in the mesoscopic regime, separating scattering attenuation from absorption. This Chapter describes two-dimensional (2D) numerical simulations of the physical system, using the spectral-element method (SEM) (e.g., Komatitsch & Tromp, 1999) to model the ultrasonic experiment with sharp topographic features, and investigate subtle details in the laboratory data on the scale of the individual scatterer (i.e. the microscopic scale).

A 2D version of the spectral-element method (SEM), mostly used and validated in seismology (e.g., Priolo *et al.*, 1994; Faccioli *et al.*, 1997; Komatitsch & Vilotte, 1998; Komatitsch & Tromp, 1999, 2002a; Komatitsch *et al.*, 2002), is used to simulate wave propagation at ultrasonic frequencies in a model that contains a large number of sharp grooves. The SEM is ideal for this purpose because of its flexibility to mesh the grooved structure based on a geometrically non-conforming mesh and also because it has been shown to be accurate to model surface waves (Komatitsch & Tromp, 1999). The simulations can be compared to measurements at every surface location, because the optical detector can record at any location on the surface of the block. The source in the simulations is the analytic solution to a Rayleigh wave (e.g., Komatitsch *et al.*, 1999) and detectors are located in a line directly in front of the source. Attenuation is so weak in aluminum that elastic simulations are meaningful.

Henceforth, I refer to the vertical component of the particle velocity measured in laboratory experiments as *data* and to the numerical results as *simulations*.

5.5 Comparing data and simulations

Let us compare data and simulations at 20 detector locations at 5-mm increments on the smooth side of the model, and on the first 42 non-grooves along a line perpendicular to the grooves (strong scattering). In both experiments, the source-detector offset for the first trace is 2 mm.

The data and simulations on the smooth aluminum surface are shown in Figure 5.3. Both panels show a large direct surface-wave arrival, followed by a reflection from the far end of the aluminum block. The wavelet in the data has some energy after the main pulse caused by ringing in the transducer. This energy is not included in the source term of the simulations. The data show little attenuation and no evidence of reflections from the sides of the block, which means that the source energy emitted has little geometrical spreading, justifying 2D elastic simulations.

Figure 5.4 shows the data (top) and simulations (bottom) for waveforms in the strong scattering case. At each groove, energy is partially reflected, causing the direct arrival to be attenuated, and the group velocity to be lowered compared to the un-scattered wave propagation, which has been shown to lead to a diffusive character of energy propagation (Scales & van Wijk, 2001). The strongest events are interfering surface waves, which look qualitatively similar in the two panels. These strong events show coherence in the sense that a single phase can be tracked from one detector location to the next, whereas for late times, scattering causes arrivals to be incoherent from trace to trace. In general, detailed differences between the numerical mesh and the grooved block are amplified at later times as a result of multiple scattering, much as in coda wave interferometry (Snieder *et al.*, 2002): waves bouncing back-and-forth numerous times between scatterers highlight errors in the numerical representation. The later events especially show greater discrepancy in amplitude, because the path-lengths for the multiply scattered events are longer than the early arrivals, so that neglecting attenuation in aluminum becomes a significant source for the difference between data and simulations.

The amplitude of the maximum correlation between data and simulations directly reflects the accuracy of the simulations: correlation of unity means that data and simulations are identical. It is our experience that discrepancies between the physical and numerical models on the order of a fraction of the size of a single scatterer have a noticeable influence on the accuracy of the simulations.

The maximum cross-correlation for the case of strong scattering is overall lower than for the experiment on the smooth side (Figure 5.5). Especially for source-detector distances greater than 90 mm from the source, small discrepancies between the physical model and numerical representation get amplified. However, the simulations are of such precision that data and simulations on a non-groove with the size on the order of 1 mm show considerably more energy at later times than traces on the thicker non-grooves. An example of this is detector 12, compared to detector 4 (Figures 5.6 and 5.7, respectively): the relatively thin ridge of aluminum under detector 12 is excited in a 300-kHz resonance (Figure 5.8). While this mode is too low in frequency to represent a trapping of energy in the non-groove, it is possible that this resonance is a flexural mode of the thin non-groove (Rossing & Fletcher,

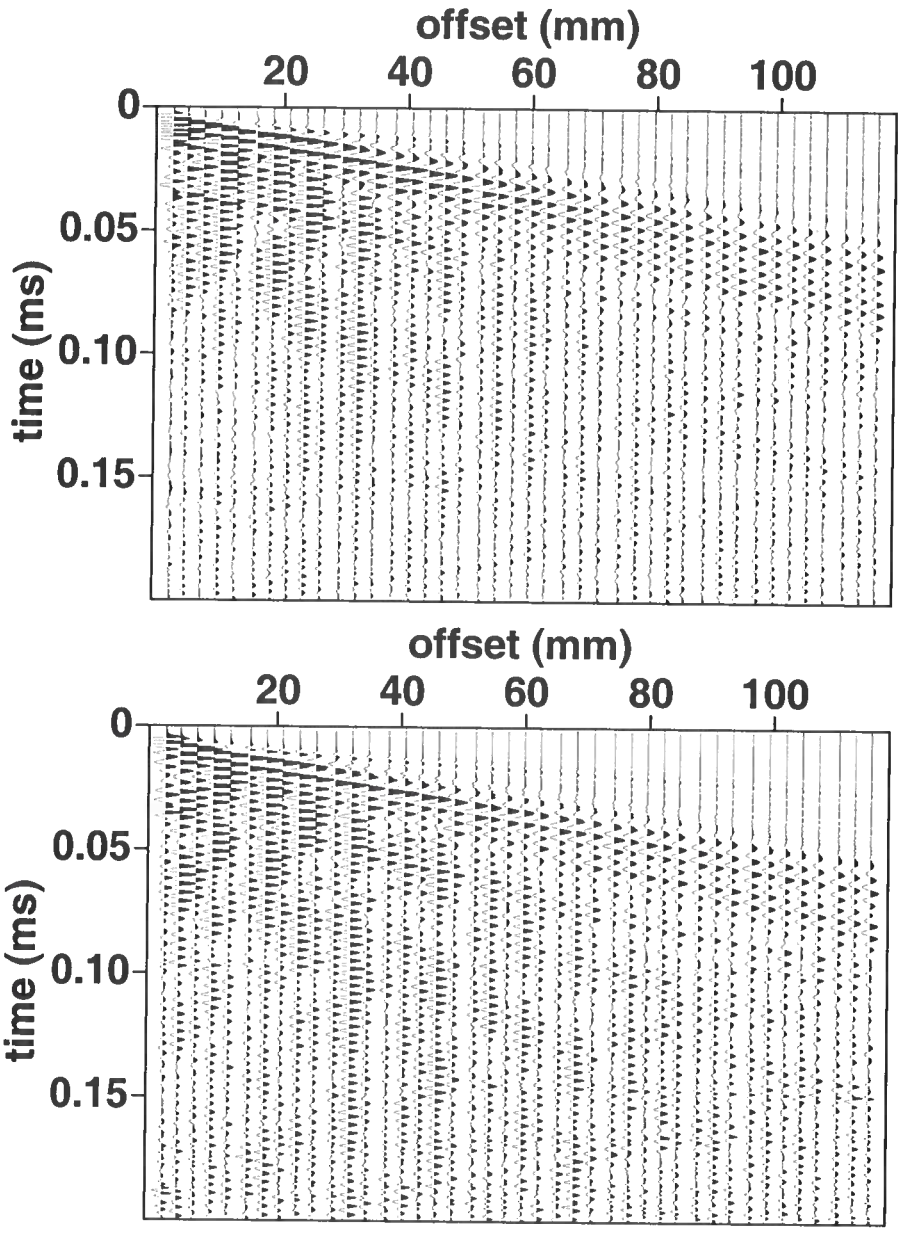

Figure 5.4. Data (top) and simulations (bottom) for wave fields on the grooved side of the model. The main energy consists of surface waves bouncing between grooves, but the small-amplitude, faster events are body-waves diffracted at the grooves.

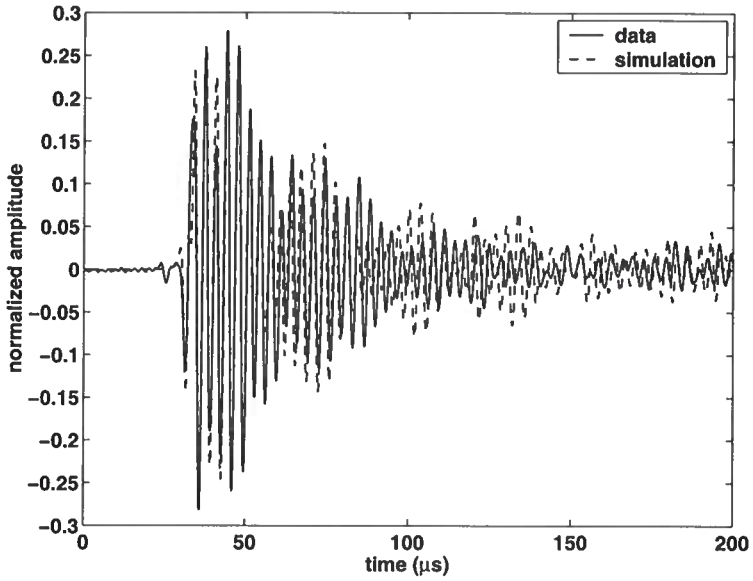

Figure 5.6. Comparison between data and simulations for detector 4 on the grooved side of the model. This detector is located on a thick non-groove.

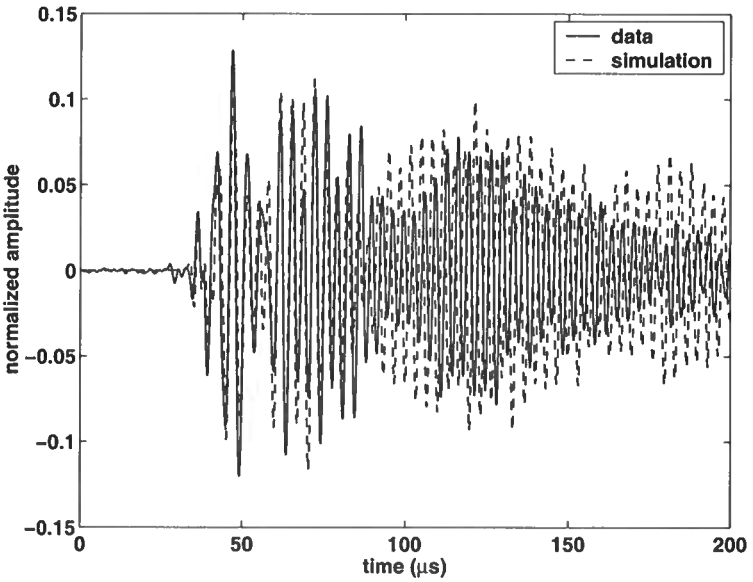

Figure 5.7. Comparison between data and simulations for detector 12 on the grooved side of the model. This detector is located on a thin non-groove. Note the relatively stronger amplitudes at later times than for detector 4.

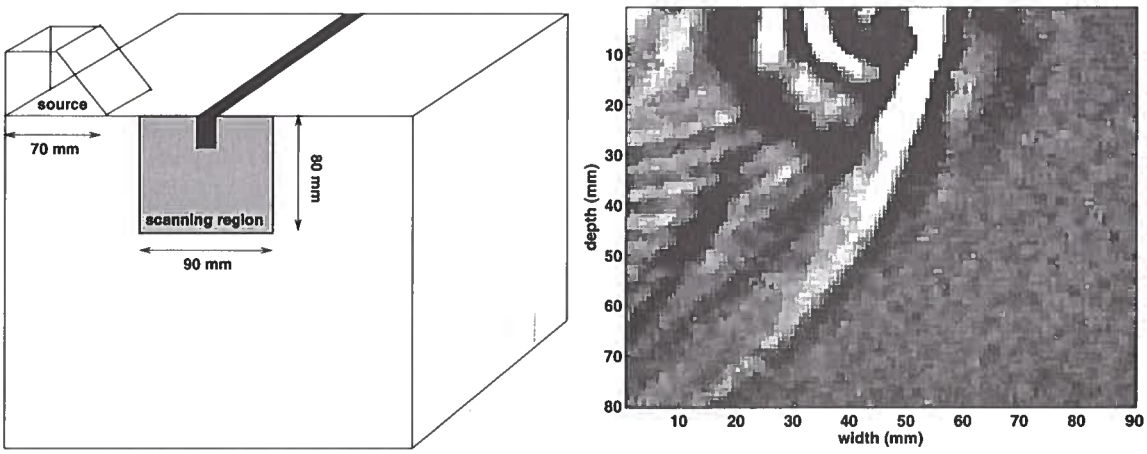

Figure 5.10. Left: experimental configuration, where the source is perpendicular to a single groove on the top of the block, while the detector scans the side. Right: snap-shot of particle motion in the scanned region after the incident field scattered off a single groove.

with a P-wave velocity cannot be seen until the 6th or 7th trace at t= 0.01 ms, but is confirmed by the simulations. These events are spherical body-wave fronts diffracted at the individual grooves, which arrive before the Rayleigh waves, and may be analogous to precursors to the seismic phase PKKP in global seismology, believed to be caused by scattering at the rough boundary between the Earth's outer-core and mantle (Earle & Shearer, 1997).

To support the existence of body-wave precursors to the surface-wave energy, a second experiment was conducted, where the source is mounted on the side of the aluminum model with a single groove, while the detector scans the side of the model (see the left panel of Figure 5.10). The right panel of Figure 5.10 shows a snap-shot of particle motion, measured shortly after the incident wave interacted with the single groove. The side of the aluminum block breaks the symmetry of the Rayleigh-wave motion purely in the x- and z-direction, creating particle motion in the $y-$direction. In the top-left corner, one can see energy due to ringing of the source, and the incident field is the (close to) linear event. The circular events are body-waves scattered off the single groove. Scattering to body waves is stronger in the backward direction, but significant P-wave energy travels ahead of the surface wave, causing the precursors observed in Figure 5.4.

5.7 Conclusions

Relatively small-amplitude features from individual scatterers are confirmed by spectral-element simulations. For example, body-wave precursors to the main surface-wave energy are caused by diffraction from the scatterers, which may be analogous to PKKP precursors, believed to be caused by scattering at the core-mantle boundary. Also, flexural resonance

Chapter 6

Measuring, imaging and suppressing scattered surface waves

6.1 Summary

Near-surface scattering can contaminate the arrival of energy from target reflectors. We developed a 3D wave-theoretical method to reduce the presence of near-surface scattering on the records, as a multi-channel alternative for short-wavelength static corrections. The method was successfully tested on laboratory data, excited and monitored with a computer controlled, non-contacting system.

6.2 Introduction

When a wave front travels through a complex overburden, it is disturbed by scattering from heterogeneities. For a detailed structural image of the deeper subsurface it is important to minimize these disturbances in arrival time and amplitude of upcoming reflections. Currently, residual static correction methods correct for rapid variations in arrival times of a reflector, but these techniques are based on a model that assigns the same uniform time shift to each trace from a distinct surface location (e.g., Wiggins *et al.*, 1976), assuming vertical ray paths through the overburden. Such corrections are usually referred to as time- and surface-consistent corrections (Taner *et al.*, 1974). Although statics techniques are based on this simple (transmission) model of the subsurface, they can be effective in many cases. However, in a strongly heterogeneous shallow subsurface, this statics model breaks down (e.g., Combee, 1994). Neglecting (multiply) scattered waves, as in the static assumption, can degrade the high-frequency content of the data, due to destructive interference of rapidly varying traces during stacking.

We estimate a surface impedance distribution of the region directly under the receivers from one particular event and subsequently predict and subtract the scattered energy for the entire record, improving resolution of the target reflectors. This method is based on an integral-equation formulation of the scattering process near the surface, developed by Delft University of Technology (Blonk & Herman, 1994; Ernst *et al.*, 2002; Campman *et al.*, 2003). We present examples based on laboratory models, where we excite and measure wave fields that are scattered at the near surface. With our non-contacting data acquisition, receiver intervals are less than the dominant wavelength, allowing us to filter in the wavenumber domain, as with the dense receiver arrays that are currently being tested in exploration

the scattered energy (i.e. a multi-channel operation).

First, we select an event:

$$v(\mathbf{x},t) = d(\mathbf{x},t) + r(\mathbf{x},t), \tag{6.3}$$

where v are the data, d is the selected event and r denotes the rest of the data. Selecting d can be done by time windowing. The window should be long enough to include scattering tails but it should not include other events. Next, we decompose the strong event $d(\mathbf{x},t)$, in a similar way as in equation (6.1):

$$d(\mathbf{x},t) = d^0(\mathbf{x},t) + d^1(\mathbf{x},t). \tag{6.4}$$

Here, d^0 is the field in the near surface that would exists without scattering and d^1 is the scattered field, excited by the incident field being scattered from heterogeneities in the near-surface. The impedance model is obtained from back-propagating the near-surface scattered energy with the Green's function derived in Campman *et al.* (2003). The impedance distribution is determined by minimizing an L^2-norm, using conjugate gradient. To set up the minimization scheme, we write equation (6.2) for a single event, in the form

$$d^1 = K\sigma, \tag{6.5}$$

where σ is the surface impedance distribution and the operator K is defined as

$$\{K\sigma\}(\mathbf{x}_l, z_0, \omega) = \int_{\mathbf{x}'_l \in \Sigma} u_z^G(\mathbf{x}_l - \mathbf{x}'_l, \Delta z, \omega)\sigma(\mathbf{x}'_l, z_1, \omega)d(\mathbf{x}'_l, z_1, \omega)\mathrm{d}\mathbf{x}'_l. \tag{6.6}$$

We then minimize the squared difference between the observed scattered field and the reconstructed scattered field, regularized by the norm of the distribution of scatterers:

$$F = \frac{||d^1 - K\sigma||^2}{||d^1||^2} + \lambda||\sigma||^2, \tag{6.7}$$

where the size of λ determines the penalty on the norm of the distribution of scatterers. By assumption, the scatterers are close to the surface so that in equation (6.6), we can substitute the field at depth z_1 with the field at z_0, leaving σ the only unknown. In contrast to Born-type imaging methods, this method accounts for multiply scattered waves.

6.5 Experiment 1: a surface wave test

We measure the wave field on the surface of an aluminum block, excited by a pulsed infrared laser (e.g., Scruby & Drain, 1990). We focused the laser beam on a line to create a line surface wave source. This wave front is scattered by a cylindrical cavity with a diameter of 2 mm and a depth of 3 mm, which is roughly the size of the dominant wavelength. The wave field is detected using a scanning laser interferometer that measures the vertical component of the particle velocity on the surface of the model via the Doppler shift (Scales

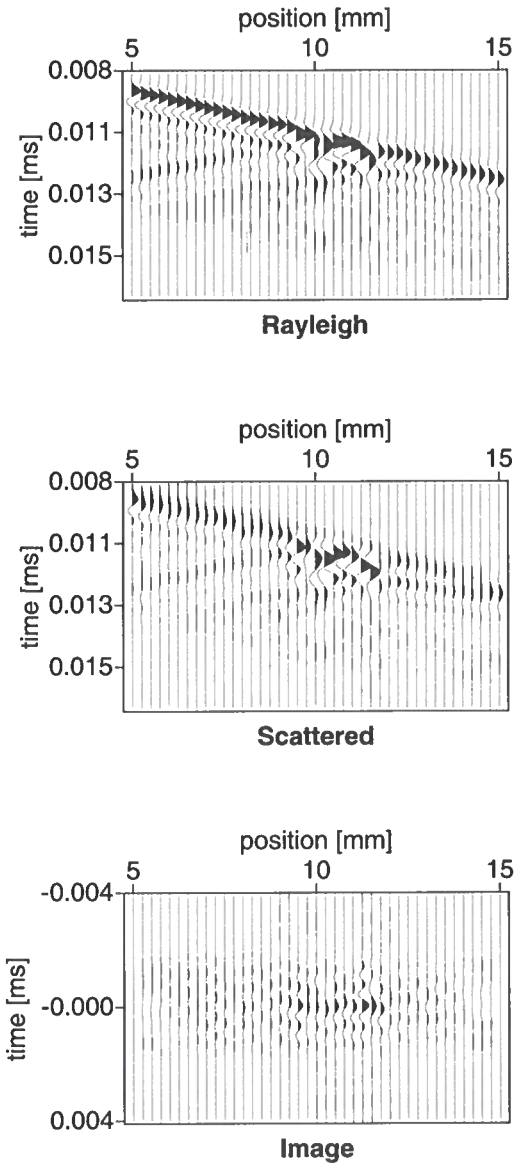

Figure 6.2. Top: part of the direct Rayleigh wave (event d in the text). This event is used to derive the scattered energy d^1. Middle: separated scattered energy, using a wavenumber frequency domain filter. Bottom: image of the cavity along the same line.

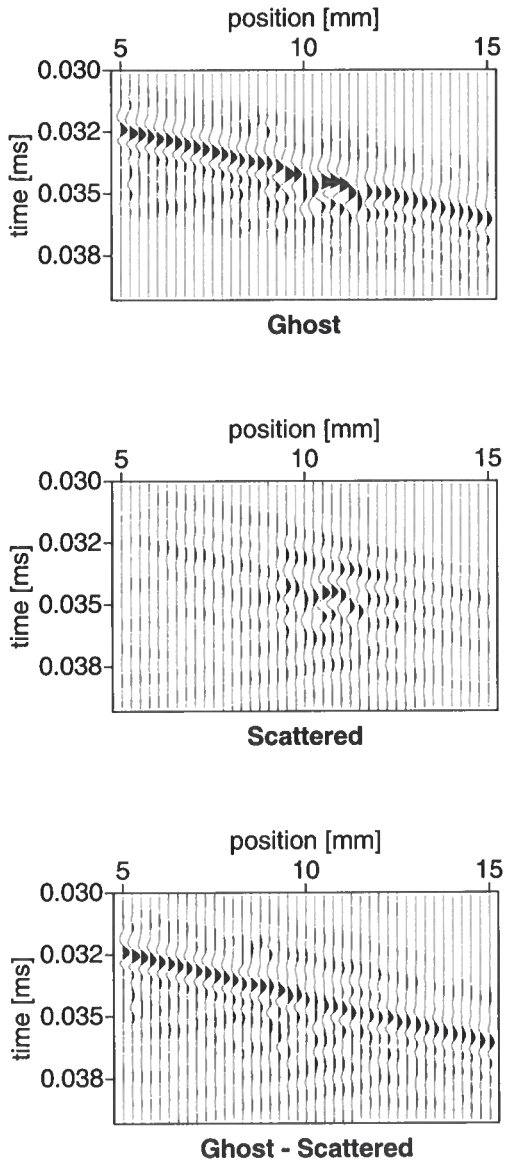

Figure 6.4. Top: the ghost Rayleigh wave. Middle: the predicted scattered field for this event. Bottom: the ghost Rayleigh wave after removing predicted near-surface scattering.

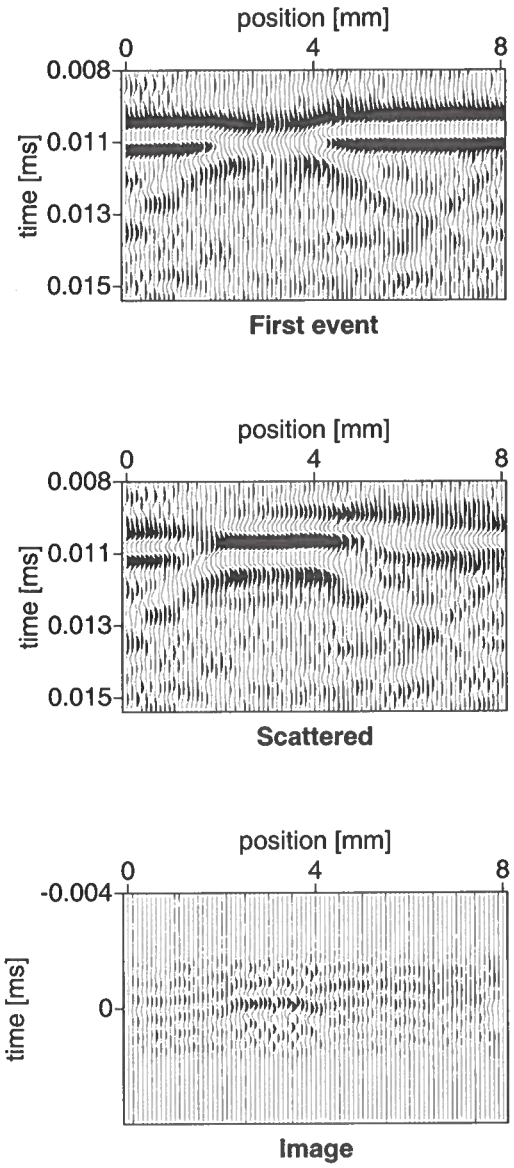

Figure 6.6. Top: the first upcoming event from the data. (event d in the text). This event is used to derive the scattered energy. Middle: separated scattered energy, d^1, using a narrow wavenumber frequency domain filter. Bottom: image of the cavity along the same receiver line.

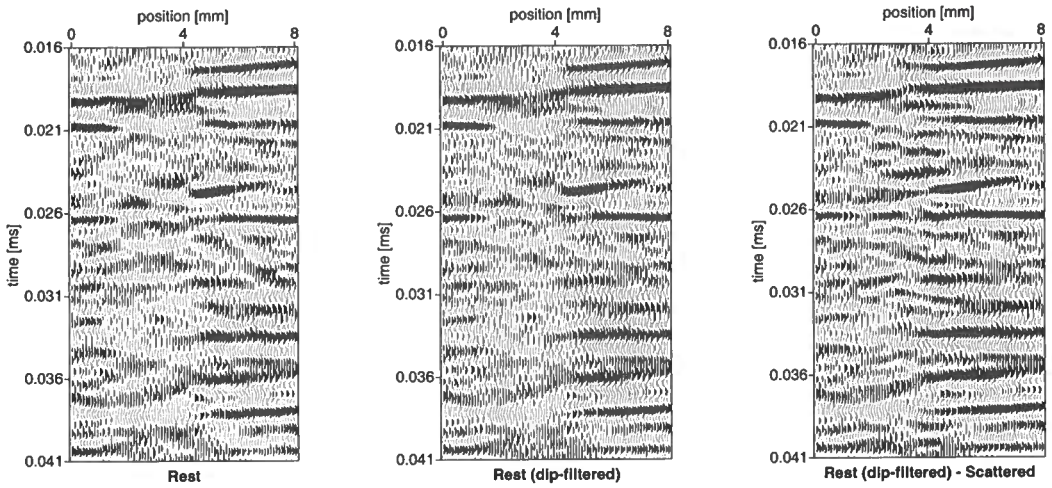

Figure 6.8. Left: part of the rest of the record. Middle: same as in the left panel but after dip-filtering to attenuate surface waves. Right: rest of the record after subtracting near-surface scattered energy and after dip-filtering.

6.7 Conclusions

We present a robust prediction-and-removal algorithm to attenuate strong near-surface scattering from seismic data. Using data from a laboratory-scale scattering experiments, we are able to estimate the surface impedance distribution using a single event. This impedance distribution is then used to predict and remove the scattered field from other events, restoring the continuity of target reflectors. A similar test on a more challenging multiple scattering experiment also gives promising results. The success of the algorithm is aided by dense 3D data acquisition, allowing filtering in the wavenumber domain.

Chapter 7

Concluding remarks

The study of our surface wave laboratory proved ideal to understand, and then exploit, wave propagation in disordered media. Tunability of the scattering strength, easy access, fast and dense acquisition in the lab and the longevity of surface waves provide a unique view *inside* the scattering medium.

Scattering induced attenuation and the decay of seismic velocities are caused by energy being transferred into the coda. These multiply scattered waves extract energy from the coherent pulse. This is why the coherent field decays exponentially due to absorption *and* scattering. It is the coherent wave that historically has been the only energy of interest in global and exploration geophysics. In medical imaging, scattering of light in biological tissue is so strong that the only recorded signal is incoherent. Their main *imaging* tool is a diffusion model. Being in the intermediate regime, where we have coherent and incoherent signal, allows a more robust medium parameter estimation. The tool of choice is radiative transfer, which describes both the coherent and the incoherent energy propagation in scattering media. Treating the scattering medium as a whole (macroscopically), medium parameters like the diffusion constant and energy velocity were revealed in scattered energy. However, in the intermediate regime, the mesoscopic scale, the treatment of the observations in terms of averaged intensity led to separate estimation of scattering attenuation and intrinsic absorption.

In higher dimensions, the radiative transfer equation becomes considerably more difficult since there are an infinite number of directions to scatter into, as compared to two directions in 1D (Paasschens, 1997). However, even in 1D, the rich character of radiative transfer is evident. Exponential decay is experienced by the direct wave due to scattering and absorption. Aspects of both wave and diffusive behavior emerge in the average total intensity, and, in the presence of both, a *mesoscopic* picture of the scattering medium can be formed.

The theory of radiative transfer has its limitations. The most severe is that it does not include wave interference. As a result of this, there exists a distance between source and receiver, known as the localization length, past which radiative transfer is incorrect. Sheng (1995) estimates that in 1D the localization length is approximately four mean free paths. This offers the possibility of an intermediate range (one to four mean free paths) where radiative transfer holds. Future work should attempt to find good bounds on this range in practice.

A direct application in geophysics of radiative transfer modeling is presented in Appendix D. Under many assumptions that need to be tested in future research, we obtain

References

Aki, K., & Chouet, B. 1975. Origin of coda waves: source, attenuation and scattering effects. *J. Geophys. Res.*, **80**, 3322–3342.

Aki, K., & Richards, P. G. 1980. *Quantitative seismology: theory and practice.* Freeman.

Anderson, H. L. (ed). 1989. *A physicist's desk reference; physics vade mecum.* 2nd edn. 335 East 45th Street, New York,NY 10017: American institute of Physics.

Anderson, P. W. 1958. Absence of diffusion in certain random lattices. *Phys. Rev.*, **109**, 1492–1505.

Asch, M., Kohler, W., Papanicolaou, G., Postel, M., & White, B. 1991. Frequency content of randomly scattered signals. *SIAM Review*, **33**, 519–625.

Backus, G. 1962. Long wavelength anisotropy. *J. Geophys. Res.*, **67**, 4427–4440.

Baeten, G., Belougne, V., Combee, L., Kragh, E., Laake, A., Martin, J., Orban, J., Ozbek, A., & Vermeer, P. L. 2000. Aquisition and processing of point receiver measurements in land seismic. *In: Expanded abstracts, 62nd Mtg.* B-06. Eur. Assn. Geosci. Eng.

Banik, N. C., Lerche, I., & Shuey, R. T. 1985. Stratigraphic filtering, Part I: Derivation of the O'Doherty-Anstey formula. *Geophysics*, **50**, 2768–2774.

Bleistein, N., Cohen, J. K., & Stockwell Jr., J. W. 2001. *Mathematics of multidimensional seismic imaging, migration and inversion.* New York: Springer-Verlag.

Blonk, B., & Herman, G. C. 1994. Inverse scattering of surface waves : A new look at surface consistency. *Geophysics*, **59**, 963–972.

Boas, D. A., Campbell, L. E., & Yodh, A. G. 1995. Scattering and imaging with diffusing temporal field correlations. *Phys. Rev. Lett*, **75**, 1855–1858.

Boyce, W. E., & DiPrima, R. C. 1997. *Elementary differential equations.* New York: Wiley.

Campillo, M., & Paul, A. 2003. Long-range correlations in the diffuse seismic coda. *Science*, **299**, 547–549.

Campillo, M., Margerin, L., & Shapiro, N. 1999. Seismic wave diffusion in the Earth lithosphere. *Pages 383–404 of:* Fouque, J.-P. (ed), *Diffuse waves in complex media.* Kluwer.

Haney, M., van Wijk, K., & Snieder, R. K. 2003. *Radiative transfer in 1D, and the connection to the O'Doherty-Anstey formula.* In CWP Project Review and submitted to Geophysics.

Hemmer, P. C. 1961. On a generalization of Smoluchowski's diffusion equation. *Physica*, **27**, 79–82.

Hendrich, A., Martinez, A. S., Maynard, R., & van Tiggelen, B. A. 1994. The role of the step length distribution in wave-diffusion. *Phys. Lett. A*, **185**, 110–112.

Hennino, R., Trégourès, N., Shapiro, N. M., L. Margerin, L., Campillo, M., van Tiggelen, B. A., & Weaver, R. L. 2001. Observation of equipartition of seismic waves. *Phys. Rev. Lett.*, **86**(15), 3447–3450.

Hess, P. 2002. Surface acoustic waves in materials science. *Physics Today*, March, 42–47.

Ishimaru, A. 1997. *Wave propagation and scattering in random media.* Oxford University Press.

Kennett, B. L. N. 1984. Guided wave propagation in laterally varying media – I. Theoretical development. *Geophys. J. R. astr. Soc.*, **79**, 235–255.

Komatitsch, D., & Tromp, J. 1999. Introduction to the spectral-element method for 3-D seismic wave propagation. *Geophys. J, Int.*, **139**, 806–822.

Komatitsch, D., & Tromp, J. 2002a. Spectral-element simulations of global seismic wave propagation-I. Validation. *Geophys. J. Int.*, **150**, 390–412.

Komatitsch, D., & Tromp, J. 2002b. Spectral-element simulations of global seismic wave propagation-II. 3-D models, oceans, rotation, and self-gravitation. *Geophys. J. Int.*, **150**, 303–318.

Komatitsch, D., & Vilotte, J. P. 1998. The spectral-element method: an efficient tool to simulate the seismic response of 2D and 3D geological structures. *Bull. Seism. Soc. Am.*, **88**, 368–392.

Komatitsch, D., Vilotte, J. P., Vai, R., Castillo-Covarrubias, J. M., & Sánchez-Sesma, F. J. 1999. The spectral element method for elastic wave equations– application to 2-D and 3-D seismic problems. *Int. J. Num. Methods in Engeneering*, **45**, 1139–1164.

Komatitsch, D., Ritsema, J., & Tromp, J. 2002. The spectral-element method, Beowulf computing, and global seismology. *Science*, **298**, 1737–1742.

Kuga, Y., Ishimaru, A., & Rice, D. 1993. Velocity of coherent and incoherent electromagnetic waves in a dense strongly scattering medium. *Phys. Rev. B*, **48**(17), 13155–13158.

Lemieux, P. -A., Vera, M. U., & Durian, D. J. 1998. Diffusing-light spectroscopies beyond the diffusion limit: The role of ballistic transport and anisotropic scattering. *Phys. Rev. E*, **57**(4), 4498–4515.

Smith, M. L., Sondergeld, C. H., & Norris, J. O. 1991. The Amoco array sonic logger. *The log analyst*, **32**(3), 201–214.

Snieder, R., Grêt, A., Douma, H., & Scales, J. A. 2002. Coda wave interferometry for estimating nonlinear behavior in seismic velocity. *Science*, **295**, 2253–2255.

Snieder, R. K. 1986. 3D Linearized scattering of surface waves and a formalism for surface wave holography. *Geophys. J. R. astr. Soc.*, **84**, 581–605.

Strutt, J. 1885. On waves propagated on the plane surfaces of an elastic solid. *Proc. London Math. Soc.*, **17**, 4–11.

Taner, M. T., Koehler, F., & Alhilali, K. A. 1974. Estimation and correction of near-surface time anomalies. *Geophysics*, **39**, 441–463.

Toet, D., Potemski, M., Wang, Y. Y., & Maan, J. C. 1991. Experimental observation of Landau levels in nonperiodic (Fibonacci) superlattices. *Phys. Rev. Lett.*, **66**(2128).

Turner, J. 1994. *Radiative transfer of ultrasound.* Ph.D. thesis, University of Illinois.

van Albada, M. P., van Tiggelen, B. A., Lagendijk, A., & Tip, A. 1991. Speed of propagation of classical waves in strongly scattering media. *Phys. Rev. Lett.*, **66**, 3132–3135.

van Rossum, M. C. W., & Nieuwenhuizen, Th. M. 1999. Multiple scattering of classical waves: microscopy, mesoscopy, and diffusion. *Rev. Mod. Phys.*, **71**(1), 313–371.

van Wijk, K., Komatitsch, D., Scales, J. A., & Tromp, J. 2003a. *Analysis of strong scattering at the micro-scale.* submitted to J. Acoust. Soc. Am.

van Wijk, K., Haney, M., & Scales, J. A. 2003b. *Energy propagation in a 1D attenuative medium in the laboratory.* Submitted to Phys. Rev. Lett.

Viktorov, I. A. D. 1967. *Rayleigh & Lamb waves. Physical theory and application.* New York: Plenum Press.

Wegler, U., & Lühr, B-G. 2001. Scattering behavior at Merapi volcano (Java) revealed from active seismic experiment. *Geophys. J. Int.*, **145**, 579–592.

Wiggins, R. A., Larner, K. L., & Wisecup, R. D. 1976. Residual statics analysis as a general linear inverse problem. *Geophysics*, **41**, 922–938.

Wolfe, J. 1998. *Imaging phonons: acoustic wave propagation in solids.* Cambridge University Press.

Wu, R. 1985. Multiple scattering and energy transfer of seismic waves– Separation of scattering effect from intrinsic attenuation–I. Theoretical modeling. *Geophys. J. R. astr. Soc.*, **82**, 57–80.

Appendix A

The angle-beam transducer source

To analyze the observations of multiply scattered waves, it is of vital importance to know the characteristics of the source. In this case, a piezo-electric crystal converts a voltage to mechanical energy, causing a compressional wave (P-wave) in a Lucite wedge, to which it is attached (see the left panel of Figure A.1). The transducer wedge has a footprint of 7 cm (in the forward direction) by 4.2 cm and is cut at an angle of 68 degrees, so that the horizontal component of the P-wave in Lucite matches the surface wave velocity in aluminum, causing the source wavelet to be predominantly a surface wave. This surface wave is otherwise known as the Rayleigh wave, named after Lord Rayleigh (J. Strutt) who showed theoretically in Strutt (1885) that waves can propagate over the plane boundary of an elastic half-space over vacuum or a gas like air. These waves have elliptical polarization, comparable to surf in the ocean. Also, their amplitude decays exponentially with depth, where the exponent is inversely proportional to its wavelength. This property of the surface wave is often exploited in near-surface characterization and global Earth seismology (Aki & Richards, 1980), where a spectral analysis assigns material properties according to the depths of penetration of the Rayleigh waves.

A.1 The source on homogeneous aluminum

The right panel of Figure A.1 shows the areas of the three areas of data acquisition. A scan of the surface of the block, where the source is located (so-called *top*), measures the vertical particle velocity of the source wavelet. The scan-area labeled *side*, provides the out-of-plane horizontal component of the source wavelet. Finally, the experiment scanning the *front* of the block, measures the out-of-plane component of the source wavelet. The source wedge is drawn on the edge of the aluminum for all three experiments, for visual purposes. This was only the location of the source, when scanning the side of the block for reasons that will become apparent in the following text. In the other two experiments, the source is away from all sides to exclude side-reflections.

Even though we have the capability to excite energy in the model in a non-contacting matter with a pulsed Nd:YAG laser (Scruby & Drain, 1990), most data are recorded with this 500-kHz Panametrics angle-beam transducer. We chose this source, because the laser source excites predominantly such short wavelengths, that the groove sequence obstructs transmission of significant energy, past a few grooves.

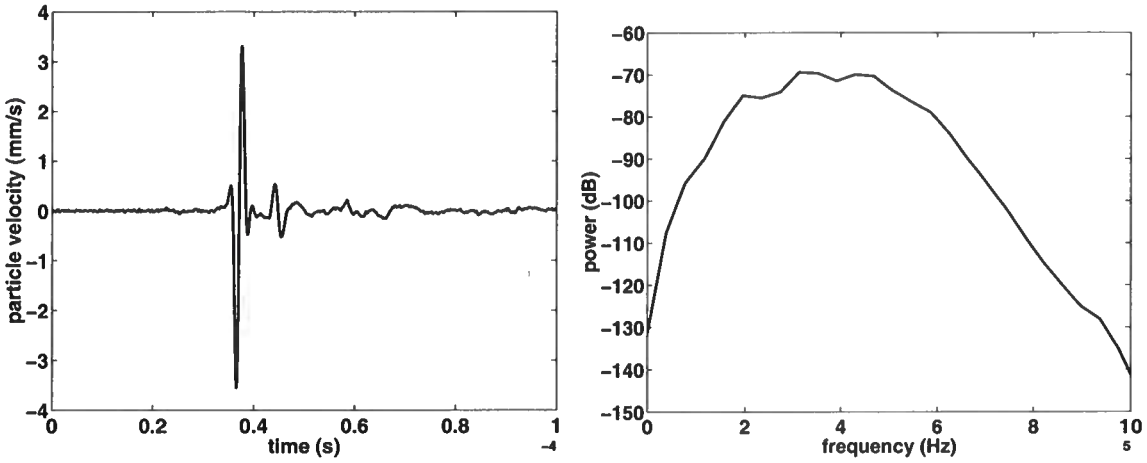

Figure A.2. Vertical component of the source wavelet, measured on the top of the block. The left panel is a single trace in front of the center of the wedge and its power spectrum is plotted on the right.

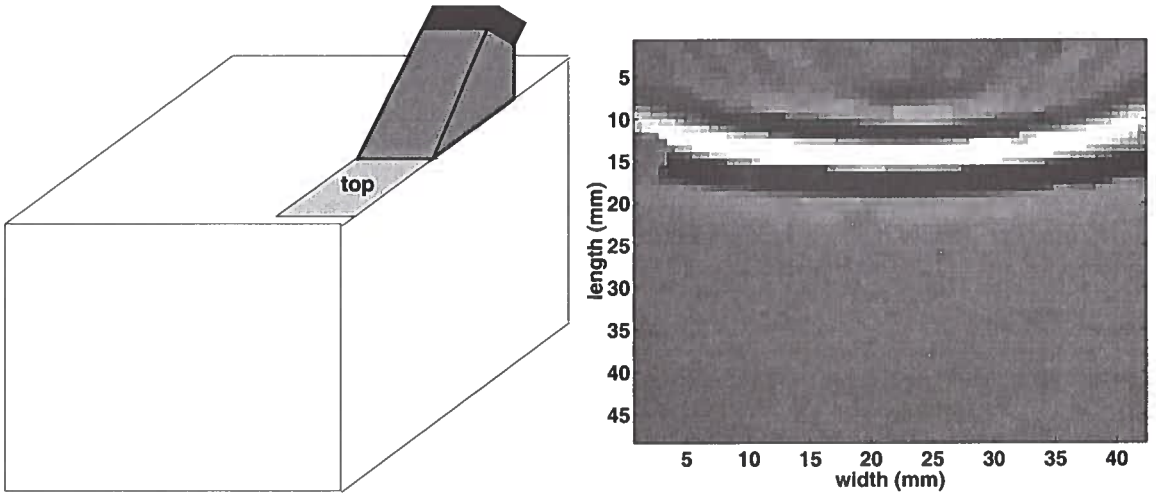

Figure A.3. Left: Experimental configuration to measure the vertical component of the source wavelet across the width of the source wedge. The right panel is a snap-shot of the experiment. Black represents large positive amplitude and white is strong, negative amplitude. The energy between the source and the main energy is ringing of the source.

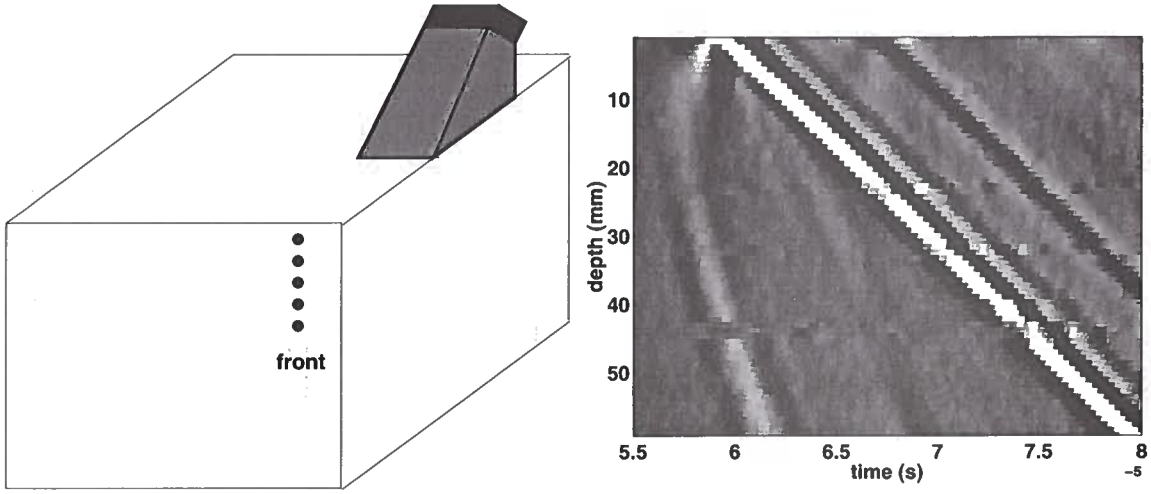

Figure A.5. Left: experimental configuration of the measurement of the in-line horizontal component of the source wavelet, measured on the end of the block, on a line of receivers down the center of the source-wedge. Right: The curved front is the direct arrival of the source wavelet, whereas the linear events are diffractions from the edge, traveling down the block.

last groove, 40 mm from the edge (Figure A.6). This last measurement can only provide a short time-window of the source wavelet on the grooves, because reflected energy off the end of the block re-enters the system. However, when we compare the source wavelet on the grooved side to a 300 kHz low-pass version of the wavelet on the smooth side of the aluminum, we see similarity that is mostly disturbed by the reflection off the back of the block later in the trace (Figure A.7). Therefore, we use the low-pass filtered source wavelet from the smooth side of the aluminum to model the ensemble measurements.

Appendix B

Insights in the radiative transfer equation

In the geophysical community, the theory of radiative transfer is relatively novel. This Appendix is an attempt to relate our results in this analysis of energy propagation to more familiar results used in exploration and global seismology.

B.1 The coherent intensity and the O'Doherty-Anstey formula

We derive results from radiative transfer that agree with results from mean field theory, namely the O'Doherty-Anstey formula. Such an equivalence suggests that radiative transfer is a proper extension of mean field theory (a "variance field" theory) for the fluctuating, multiply-scattered waves. In the field of exploration geophysics, a well known result for waves multiply scattered by a 1D layering is that obtained by O'Doherty & Anstey (1971). The O'Doherty-Anstey formula has subsequently been derived from mean field theory (Banik *et al.*, 1985). One outcome of O'Doherty-Anstey is that the amplitude of a wave transmitted through a stack of layers decays exponentially with distance as (Shapiro & Zien, 1993):

$$|T| \sim \exp(-\tilde{R}(k)x), \tag{B.1}$$

where $\tilde{R}(k)$ represents the power spectrum of the average reflection coefficient series normalized by two-way travel distance (Banik *et al.*, 1985). From the solution for the total intensity obtained in the last section, equation (4.23), radiative transfer also predicts an exponential decay for the transmitted, or coherent, wave with distance:

$$|T| \sim \exp(-Bx/2\ell_s), \tag{B.2}$$

where the distance x has replaced vt in equation (4.23) since the δ-function is only non-zero at $x = vt$. The factor of $1/2$ in the exponent of this equation shows up since radiative transfer predicts decay of the transmitted intensity - the square of the true transmission coefficient. We investigate the equivalence of these two theories for the transmission of normally incident waves through assemblages of weak 1D point scatterers (thin beds). The two theories are equivalent if:

$$\tilde{R}(k) = B/2\ell_s. \tag{B.3}$$

Depicted in Figure B.1 is the random medium we will consider: a series of thin layers of varying strength are embedded in a constant velocity background medium. In the parlance of O'Doherty-Anstey, this would be called a "cyclic" sequence. It happens to be the type

For thin layers, $kh \ll 1$ and a first order Taylor series expansion in h leads to $1-\exp(2ikh) \approx -2ikh$. Pulling it out of the summation yields

$$\tilde{R}(k) = \frac{4k^2h^2}{2L}\left|\sum_{j=1}^{N} R_j \exp\left(2ikd_j\right)\right|^2 . \tag{B.7}$$

We now use a standard argument from the theory of multiple scattering: if d_j, the spacing of the thin beds, is a random variable, the cross terms in the square of the summation in equation (B.7) cancel in the *average* and the squaring can be brought inside the summation:

$$\tilde{R}(k) = \frac{2k^2h^2}{L}\sum_{j=1}^{N} |R_j \exp\left(2ikd_j\right)|^2 . \tag{B.8}$$

Now, inside the summation, the exponential does not contribute to the magnitude and we are left with

$$\tilde{R}(k) = \frac{1}{2L}4k^2h^2\sum_{j=1}^{N}|R_j|^2 = \frac{1}{L}2k^2h^2N\langle|R_j|^2\rangle, \tag{B.9}$$

where $\langle|R_j|^2\rangle$ is the mean-square of the interface reflection coefficients.

Returning to equation (B.3), to prove that radiative transfer and the O'Doherty-Anstey formula predict the same exponential decay for the transmitted wave, we set equation (B.9) to:

$$\frac{B}{2\ell_s} = \frac{1}{L}2k^2h^2N\langle|R_j|^2\rangle. \tag{B.10}$$

For (Rayleigh) point scatterers in 1D, the radiation is isotropic. Hence, $B = 0.5$. Rearranging equation (B.10):

$$\ell_s = \frac{1}{8k^2h^2\langle|R_j|^2\rangle\frac{N}{L}}. \tag{B.11}$$

The quantity N/L is simply the number density of the thin beds, ρ. In the limit of weak scatterers (such that $R_j \ll 1$) $8k^2h^2\langle|R_j|^2\rangle = \sigma_s$, the scattering cross section (see Section B.2). The presence of weak reflection coefficients is an underlying assumption in the O'Doherty-Anstey result (Banik *et al.*, 1985), so that equation (B.11) can now be rewritten in a familiar form:

$$\ell_s = \frac{1}{\rho\sigma_s}. \tag{B.12}$$

This is recognized as equation (4.4), the independent scattering approximation. Equation (B.12) demonstrates that, for this model, the exponential decay of the transmitted wave from O'Doherty-Anstey, or mean-field theory, is equivalent to that predicted by radiative transfer. A conceptual diagram of this equivalence is shown in Figure B.2. From mean field theory, both the phase and the amplitude of the transmitted wave can be obtained; however, the incoherent energy, for which the mean is zero, falls out. Similarly, 1D radiative transfer can address the amplitude of the transmitted wave and the behavior of

a small parameter. This is the case of a small reflection coefficient. For an assemblage of thin beds with varying velocities, α represents the RMS perturbation from the background velocity. Substituting this relation for c into equation (B.13):

$$\sigma_s(k) = \frac{1}{2}k^2h^2(1-(1+\alpha)^2)^2. \tag{B.15}$$

Keeping the lowest order term in α:

$$\sigma_s(k) \approx 2k^2h^2\alpha^2. \tag{B.16}$$

To satisfy equation (B.3), we need to show that the scattering cross section in the weak scattering limit, equation (B.16), is equal to $8k^2h^2R^2$. From equation (B.14), we know that

$$8k^2h^2R^2 = 8k^2h^2\left(\frac{c-c_0}{c+c_0}\right)^2. \tag{B.17}$$

Substituting $c = c_0(1+\alpha)$ into equation (B.17) gives

$$8k^2h^2R^2 = 8k^2h^2\left(\frac{\alpha}{2+\alpha}\right)^2. \tag{B.18}$$

Again, keeping the lowest order term in α, we obtain that the right-hand side of equation (B.18) equals $2k^2h^2\alpha^2$, identical to equation (B.16). Hence, in the weak scattering limit for thin beds, $8k^2h^2R^2 = \sigma_s$.

B.3 The Green's function for the directional intensity

Expressions (4.10) and (4.11) show that the 1D radiative transfer equation can be split into a system of PDEs in terms of the left and right-going intensities. So far, only the reduced PDE governing the total intensity has been studied. This is due to the fact that measuring either the left or right-going intensity entails splitting the wave field into left and right-going waves. Such a decomposition requires dense spatial sampling to perform the type of filtering routinely done in Vertical Seismic Profiling: separating up from down-going waves. Here, we show that knowledge of the individual left and right-going energies can give us more detailed insight into the incoherent energy.

Assuming that the wave field has been decomposed into left and right-going waves, we now solve the system of 2 partial differential equations that comprise the full radiative transfer equation. To begin, we write equations (4.10) and (4.11) in matrix form:

$$\frac{\partial \mathbf{I}}{\partial t} + M\frac{\partial \mathbf{I}}{\partial x} = N\mathbf{I} + \mathbf{S}, \tag{B.19}$$

To get the directional intensities in the spatial domain, we must inverse Fourier transform equations (B.24) and (B.25). Two identities are needed for this inversion:

$$ix \int_{-\infty}^{\infty} \tilde{I}(k) \exp(-ikx) dk = \int_{-\infty}^{\infty} \frac{\partial \tilde{I}(k)}{\partial k} \exp(-ikx) dk, \tag{B.26}$$

and from the theory of Bessel functions (Hemmer, 1961):

$$\int_{-\infty}^{\infty} \cos(kx) \frac{\sin\left(t\sqrt{k^2v^2 - \frac{B^2}{\tau_s^2}}\right)}{\sqrt{k^2v^2 - \frac{B^2}{\tau_s^2}}} dk = \frac{\pi}{v} I_0 \left[\frac{B}{\ell_s}\sqrt{v^2t^2 - x^2}\right] u(vt - |x|). \tag{B.27}$$

After inverting the Fourier transform, we obtain for the right-going intensity:

$$\begin{aligned} I_r(x,t) = \quad & \frac{1}{4} \exp\left(-Bvt/\ell_s\right) \exp\left(-vt/\ell_a\right) \left[2(1+c)\delta(vt-x) + \frac{B}{\ell_s} u(vt - |x|) \times \right. \\ & \left[(1-c) I_0\left(\frac{B}{\ell_s}\sqrt{v^2t^2 - x^2}\right) + \right. \\ & \left.\left. (1+c)\sqrt{\frac{vt+x}{vt-x}} I_1\left(\frac{B}{\ell_s}\sqrt{v^2t^2 - x^2}\right)\right]\right], \end{aligned} \tag{B.28}$$

and for the left-going intensity:

$$\begin{aligned} I_r(x,t) = \quad & \frac{1}{4} \exp\left(-Bvt/\ell_s\right) \exp\left(-vt/\ell_a\right) \left[2(1-c)\delta(vt+x) + \frac{B}{\ell_s} u(vt - |x|) \times \right. \\ & \left[(1+c) I_0\left(\frac{B}{\ell_s}\sqrt{v^2t^2 - x^2}\right) + \right. \\ & \left.\left. (1-c)\sqrt{\frac{vt-x}{vt+x}} I_1\left(\frac{B}{\ell_s}\sqrt{v^2t^2 - x^2}\right)\right]\right], \end{aligned} \tag{B.29}$$

These equations for the two intensities show that the two Bessel functions that make up the incoherent intensity are sensitive to different aspects of the source radiation pattern. For instance, if the source were unidirectional, $c = -1$ or $c = 1$ and the zero order Bessel function would come from one direction and the first order Bessel from the other. It can also be verified that adding equations (B.28) and (B.29) gives the total intensity, equation (4.23). In the absence of phase information, perhaps the directional intensities can yield important information about spatial variations in the material properties.

B.4 The diffusion approximation in infinite 1D media

At late times, we demonstrate that radiative transfer can be simplified even further by approximating its behavior as the solution to a diffusion equation. Results of finite-difference

It is common to relate ℓ_{tr} to ℓ_s via:

$$\ell_{tr} = \frac{\ell_s}{1 - \langle cos\theta \rangle}, \tag{B.34}$$

where $\langle cos\theta \rangle$ represents the average scattered energy in all directions weighted by the cosine of that direction. For isotropic scattering, $\langle cos\theta \rangle = 0$ and the two mean free paths are identical. However, using the general relation $\langle cos\theta \rangle = F - B$ (Hendrich *et al.*, 1994) and the fact that $F + B = 1$, equation (B.34) can be rewritten as

$$\ell_{tr} = \frac{\ell_s}{1 - F + B} = \frac{\ell_s}{2B}, \tag{B.35}$$

which is exactly the relationship we have derived from the diffusion approximation.

B.5 The diffusion approximation in finite 1D media

The above derivation of the diffusion approximation showed how the solution of the radiative transfer equation approaches that of the diffusion equation at late times. In this section, we prove that the underlying governing equation for the total intensity at late times also becomes the diffusion equation. While the radiative transfer equation cannot be analytically solved for in a finite geometry, its late time equivalent – the diffusion equation – can be solved with boundary conditions.

Neglecting absorption ($\ell_a \to \infty$), we can rearrange equation (4.13) as

$$\frac{\partial I_n}{\partial t} + \frac{2B}{\tau_s} I_n = -v \frac{\partial I_t}{\partial x}. \tag{B.36}$$

In the diffusive regime, we assume that (Morse & Feshbach, 1953):

$$\frac{2B}{\tau_s} I_n \gg \frac{\partial I_n}{\partial t}, \tag{B.37}$$

meaning that the time rate of change of the right and left-going intensities is relatively small. Under this condition, equation (B.36) becomes

$$\frac{2B}{\tau_s} I_n = -v \frac{\partial I_t}{\partial x}. \tag{B.38}$$

Substituting equation (B.38) into equation (4.12) for I_n yields

$$\frac{\partial I_t}{\partial t} + v \frac{\partial}{\partial x} \left[-\frac{\tau_s v}{2B} \frac{\partial I_t}{\partial x} \right] = 0. \tag{B.39}$$

Under the assumption that v and τ_s do not depend on position, equation (B.39) takes the

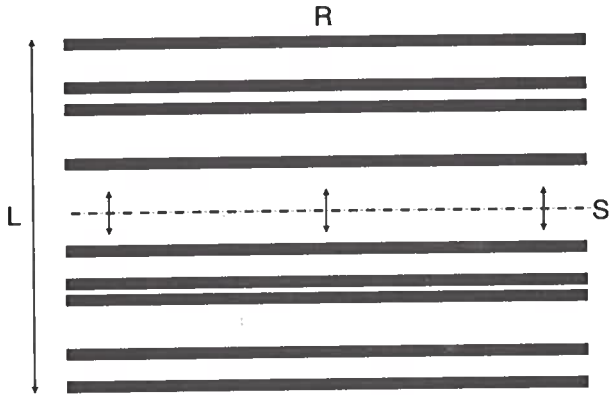

Figure B.3. The geometry of the 1D numerical scattering experiments. The source was at the center of a region with thin random layers and a receiver was positioned above the layers for each experiment. The size L of the scattering region varied between experiments with the values 80 m, 120 m, 160 m, 200 m, and 240 m.

B.6 Green's function for diffusion in an infinite 1D medium

To find the Green's function, I solve the 1D diffusion equation with attenuation using a delta function source:

$$\frac{\partial I}{\partial t} - D\frac{\partial^2 I}{\partial x^2} + D\kappa^2 I = \delta(x)\delta(t), \tag{B.47}$$

where D is the diffusion constant, $\delta(x)\delta(t)$ the source term, and κ an absorption coefficient, caused by diffraction from the bottom of the grooves. In the (ω, k) domain, it follows that:

$$I(\omega, k) = \frac{1}{D(k^2 + \kappa^2) - i\omega}, \tag{B.48}$$

so the intensity as a function of space and time is

$$\begin{aligned} I(t,x) &= \frac{1}{(2\pi)^2}\int_{-\infty}^{\infty}\int_{-\infty}^{\infty}\frac{\exp(-ikx)\exp(-i\omega t)dkd\omega}{D(k^2+\kappa^2)-i\omega} \\ &= \exp\left(-\frac{x^2}{4Dt} - D\kappa^2 t\right)(4\pi Dt)^{-1/2}. \end{aligned} \tag{B.49}$$

We first integrate over frequency:

$$\int_{-\infty}^{\infty}\frac{\exp(-i\omega t)}{\alpha - i\omega}d\omega = 2\pi\exp(-\alpha t), \tag{B.50}$$

Appendix C

Wave speeds in scattering media

When considering wave propagation in a scattering medium, we can define the phase, group and energy (or transport) velocity, but how do these relate to the speeds of the coherent and incoherent signal from ensemble measurements? Factors are the size (van Albada *et al.*, 1991) and density (Cowan *et al.*, 1998) of the scatterers, compared to the wavelength of the signal, for instance. Here we try to unravel the different speeds, to avoid mistakes in modeling observations in the lab.

In the radiative transfer equation, there is a single velocity parameter. This is generally called the energy or transport velocity. Is it:

1. the group velocity,
2. the move-out of the envelope of the wave field with increasing source-detector offset, or
3. the move-out of the coherent signal with increasing source-detector offset?

Note that the last two are only different in the sense that the coherent signal is the ensemble average of 2.

C.1 Group velocity

By definition, the group velocity is

$$v_g = \frac{d\omega(k)}{dk}. \tag{C.1}$$

There is an obvious relation between the group and the phase velocity c:

$$v_g = k\frac{dc}{dk} + c(k), \tag{C.2}$$

from which it can be determined what we already knew: in the absence of dispersion (c is frequency independent), the group velocity *is* the phase velocity. Note also, that for negative dispersion, the group velocity can be greater than the phase velocity.

The velocity of the energy package can be described by following the envelope of the trace as it moves out with increasing source-detector offset. In seismology, it is common practice to determine the group velocity in this manner. More detailed information about

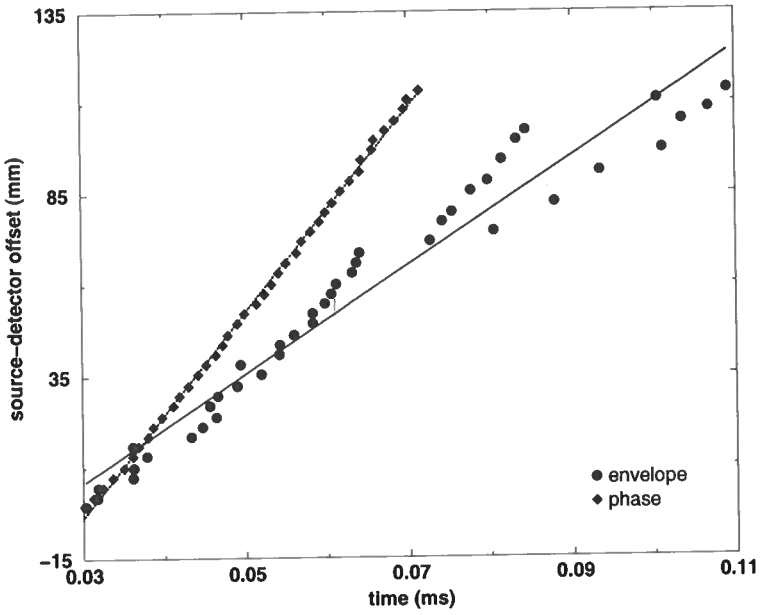

Figure C.1. Picks for a single phase and for the peak of the envelope of each surface-wave field. The straight lines are their respective regressions.

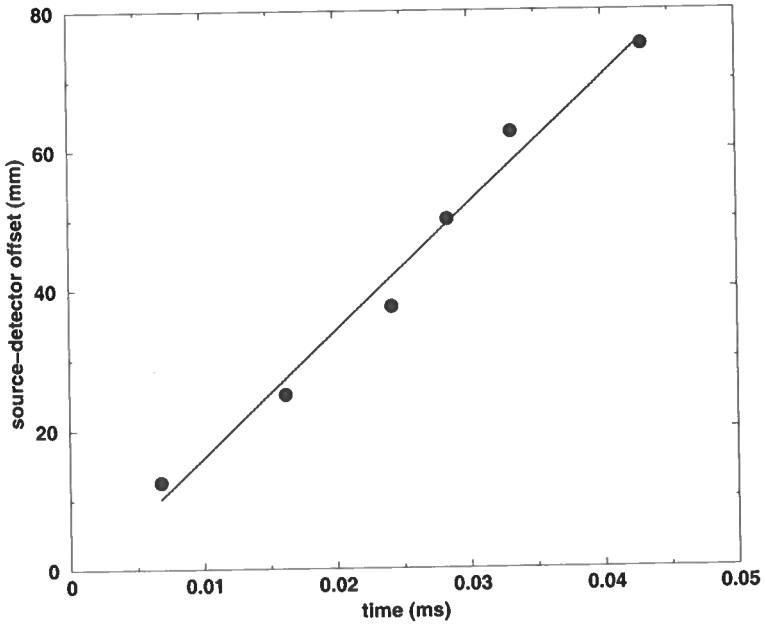

Figure C.2. Regression on the move-out of the peak of the coherent energy. The regression estimates $v_e = 1818 \pm 123$ m/s.

Appendix D

scattering attenuation and absorption in sonic logging

Intrinsic absorption in geophysical data is of great interest to the geophysical community, because it is generally considered a direct fluid indicator. However, geophysical data is attenuated by absorption *and* scattering (Scales & van Wijk, 1999). Unraveling this combination of parameters is not easy, but radiative transfer models suggest opportunities to accomplish just that. In a full-waveform sonic log, the radiative transfer model (van Wijk *et al.*, 2003b) leads to estimates of scattering attenuation and absorption, separately. This study is done on a data set of unknown location, just to show the feasibility of the method. Tying the results to geology is left to future studies.

D.1 Observations

The sonic tool has a pressure source and 8 hydrophones at 8-inch spacing (Smith *et al.*, 1991). There are 100 shot locations, 3 inches apart. Figure D.2 shows one common-shot (left) and one common-receiver record (right). On the common-shot record one can identify, from early times to late:

1. the trigger (no move-out),
2. the P-wave propagating at 4373 m/s,
3. the S-wave propagating at 2133 m/s, shortly followed by
4. the Stoneley wave, and
5. multiples between these coherent events and after the Stoneley wave.

The (multiples of) Stoneley waves can also be viewed as some normal modes of the bore-hole, or they can be treated as waves bouncing around in the vertical direction. Either way, they sample a mix of the content of the bore-hole and surrounding medium (Figure D.1).

D.2 Radiative transfer

The ensemble average of the intensities satisfies the model of radiative transfer. With only one realization of the medium at hands (Earth), we assume ergodicity in the geology and treat the stack of common-receiver sections as our ensemble average: the total intensity

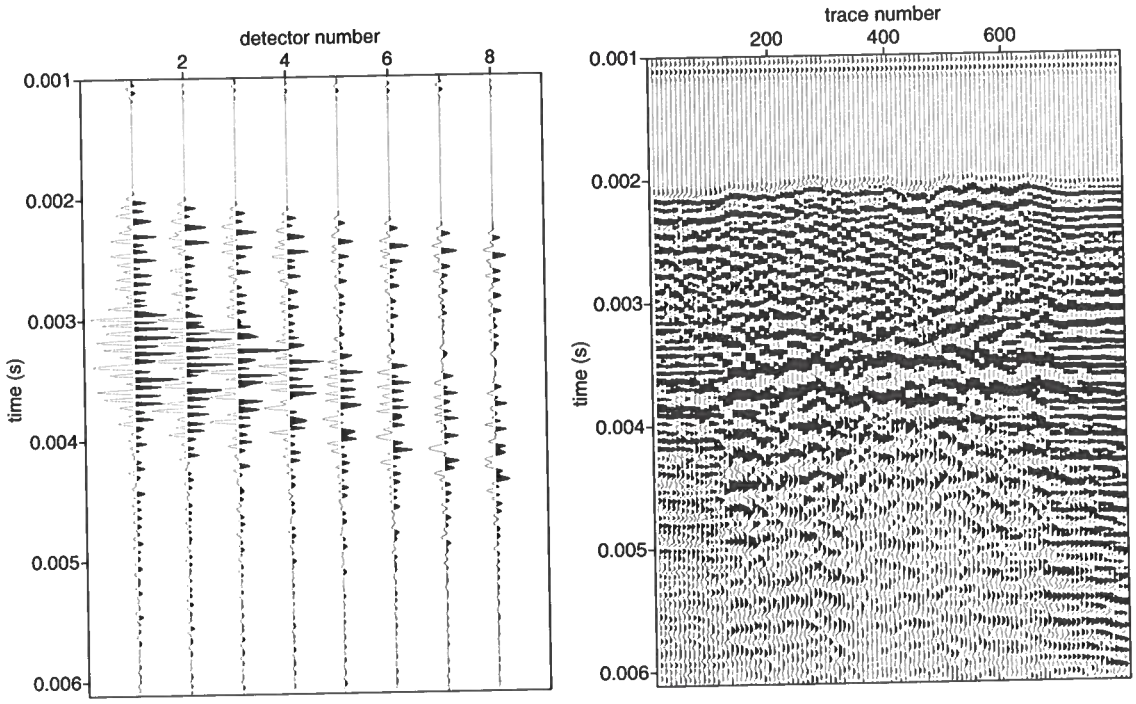

Figure D.2. Slices of the data volume. The left plot is a common-shot record and the right is a common-receiver record. Note that the recorded energy at 0.006 s is still significantly above the background noise level.

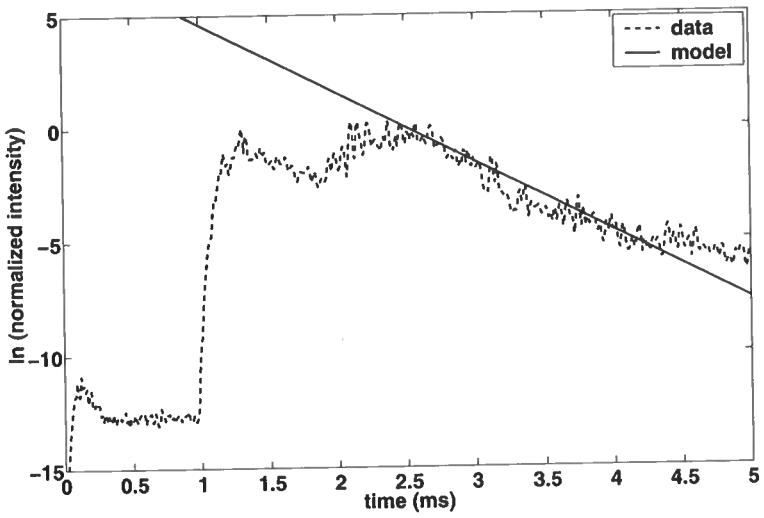

Figure D.4. The dashed line is the incoherent intensity for receiver 4. The solid line is the estimate of the incoherent intensity obtained with radiative transfer, for scattering attenuation $Q_s = 250$ and intrinsic absorption $Q_a = 10$.

with a 5 percent variance in the estimate. From fitting the incoherent intensity, we find that

$$l_s/R = 10 \text{ m} \quad \text{and} \quad l_a = 0.4 \text{ m},$$

where the variance in the estimate of the scattering mean free path is 2 percent. Especially the estimate of the absorption is very sensitive to small changes, suggesting it is well resolved. Estimates with the other 7 receivers give the same numbers, but are left out to not clutter this study.

D.3.1 Relating to Q

Relating the mean free paths to the quality factor Q, which is defined as a decay-rate per cycle, we find that

$$Q = \frac{2\pi f l}{v}. \tag{D.1}$$

This means that $Q_a = 10$ and $Q_s = 250$, which are not un-physical values, but need further studies to determine the validity. However, the variance in these estimates is less than 5 percent, suggesting the estimate is stable. The bias in these estimates are left for future studies: How bad is the 1D assumption? What part of the energy travels only through the borehole, instead of the formation?

Note that the incoherent P-wave energy displays a similar decay, so maybe the same analysis as presented here for the S-waves can be performed on it.

Appendix E

The angle-beam transducer source

Recent research has shown that the view of ray paths propagating through anomalies in the Earth are the ones most influenced by this anomaly, is not correct. In fact, these rays return to their unperturbed stage after several wavelengths, while the rays off to the side of the anomaly are perturbed most. This has potentially large implications in ray-based imaging. Laboratory data supports this view and provides a tool to further analyze this behavior called wave-front healing (Nolet & Dahlen, 2000).

A plane surface wave hits a scatterer roughly the size of the dominant wavelength (Figure E.1). We have 81-by-81 receivers in the 20-by-20 mm^2 shaded region, but shown in Figure E.2 are two cross-lines of data. Line 1 is close to the scatterer, while line 2 is roughly three wavelengths past the scatterer. Disturbances on the plane wave are visible on line 2, but the wavefront has *healed* directly behind the scatterer. We have 40 lines of data between lines 1 and 2, so we can *track* the healing process, to see if the wavefront behaves as predicted in the theory of Nolet & Dahlen (2000).